Tunable multifunctional fish-bone elastic metasurface for the wavefront manipulation of the transmitted in-plane waves

Si-Min Yuan, A-Li Chen, Liyun Cao, Hua-Wei Zhang, Shi-Wang Fan, B. Assouar, Yue-Sheng Wang

Journal of Applied Physics

AIP Publishing

Tunable multifunctional fish-bone elastic metasurface for the wavefront manipulation of the transmitted in-plane waves

Si-Min Yuan[a,b], A-Li Chen[a,*], Liyun Cao[b], Hua-Wei Zhang[a], Shi-Wang Fan[a,b], Badreddine Assouar[b,*], Yue-Sheng Wang[a,c]

[a]*Institute of Engineering Mechanics, Beijing Jiaotong University, Beijing 100044, China*

[b]*Institut Jean Lamour, CNRS, Université de Lorraine, Nancy 54000, France*

[c]*Department of Mechanics, Tianjin University, Tianjin, 300350, China*

*corresponding authors: badreddine.assouar@univ-lorraine.fr & alchen@bjtu.edu.cn

ABSTRACT

In this work, a tunable fish-bone elastic metasurface is used to manipulate the in-plane waves which are more complex than flexural or out-of-plane waves because of the coupling of the P- and SV-waves. First, the refracted generalized Snell's law (GSL) for mixed in-plane wave is deduced which is also testified by the numerical results. Then according to the GSL, the elastic metasurfaces are designed to realize multifunctions such as directional refraction and wave focusing for different working frequencies. The critical refraction is discussed for the directional refraction and the behavior of SV-wave is predicted when the P-wave is designed to focus at any point by the metasurface.

Keywords: Tunable; elastic metasurface; in-plane wave; Generalized Snell's law; simultaneous manipulation; multifunctions.

1. Introduction

Manipulating elastic waves propagating along a desired way has attracted a lot of substantial attentions. The metamaterials proposed in the recent years provide new ideas and methods for controlling of the elastic waves [1-3]. However, metamaterials cannot meet the increasing requirements of integration and miniaturization in modern devices because of their bulky and heavy characteristics. The recently proposed concept, metasurface, a kind of ultrathin metamaterial, provides broad prospects for elastic wave manipulation. It is compact, easily fabricated, and taking up less physical space than three-dimensional (3D) metamaterials [4]. It can modulate elastic waves by modifying their phase states in a predefined and desired manner based on the generalized Snell's law (GSL) [5]. For the first time, the conception of the metasurface was proposed in optics [6, 7] and then extended to acoustics [8, 9]. Up to now, significant progress has been made in the research of both kinds of metasurfaces. They have exhibited extraordinary wave manipulating properties absent in natural materials, such as anomalous reflection and refraction [10-12], self-accelerating beams [13-16], focusing [17-22] and so on. Recently, the extension to elastic metasurface has received wide attention from researchers.

The studies of elastic metasurfaces can be classified according to the types of elastic waves (out-of-plane wave, in-plane wave and surface wave). Zhu and Semperlotti [23] have presented the first numerical and experimental demonstration of elastic metasurfaces with geometric tapers to manipulate the phase profiles of Lamb waves. After then, flexural wave metasurfaces have become a research hotspot due to the wide applications of flexural waves in engineering. Such as the source illusion of flexural waves with a zigzag-shaped metasurface [24], steering flexural waves with the

metasurface constituted by the thin composite beams [25], and retroreflecting of a flexural wave with a simplified designed elastic metasurface [26]. Cao et al. also did a lot of works on flexural wave regulation, such as realizing flexural wave deflection [27-29], flexural wave asymmetric transmission [30], and flexural wave absorption [31]. As for the in-plane wave metasurface, Hu's team has designed a composite-plate-based metasurface that can steer the wavefront of SV-waves [32]; and the asymmetric transmission can be achieved by combining this kind metasurface with phononic crystals [33]. Lee et al. [34] have designed metasurfaces with the mass-stiffness substructure to realize anomalous steering and focusing of in-plane longitudinal waves. Furthermore, some works have reported on manipulating in-plane P- and SV-waves simultaneously, e.g. splitting of P-wave and SV-wave [35, 36], converting P-wave to SV-wave [37] and manipulating multimodal ultrasonic guided waves [38]. Recently, topology optimization has been used to manipulate longitudinal and shear waves [39]. Besides, the surface wave metasurface with a non-resonant meta-ridge was proposed to deflect Rayleigh surface waves [40].

However, the aforementioned elastic metasurfaces are untunable, i.e., it can only operate for a fixed or an extremely narrow frequency range, which will limit their application [41]. Hence, it is of practicale importance to study the continuously tunable elastic metasurface [42-45]. Li et al. [42] and Chen et al. [43] used piezoelectric materials to achieve the tunability of the lamb wave and flexural wave, respectively. And a tunable electromechanical resonant metasurface is proposed to steer SH waves in a plate [44]. In our previous work, a switchable multifunctional fish-bone elastic metasurface was proposed to manipulate the transmitted flexural waves [45]. In the present research, the transmitted P- and SV-waves will be manipulated simultaneously at a wide frequency range based on the tunable structure. In other words, the metasurface can be designed at each frequency within a frequency band to realize the manipulation of in-plane waves by changing the screw-in depth for different frequencies. Different from the flexural wave, the coupling between P- and SV-waves needs to be considered in the case of the in-plane waves where the relation between the phase changes for the P- and SV-waves is unknown. We first derive the generalized Snell's law for the in-plane waves and then numerically observe the phase shift and transmittance of the functional units. In addition, the mechanism of phase-shift tunability is revealed analytically. The designed metasurface can be designed to manipulate P- and SV-waves simultaneously.

2. The refracted generalized Snell's law of the mixed in-plane wave

First, we need to get the generalized Snell's law of the refracted waves in case of the mixed in-plane modes. As shown in Fig. 1, the surface $x = 0$ between media A and B is the metasurface which provides the phase shifts $\Delta\phi_P$ and $\Delta\phi_{SV}$ for P- and SV-waves, respectively. The displacements of the incident P- or SV-wave in medium A are assumed as

$$\begin{aligned} \boldsymbol{u_P} &= \boldsymbol{A_P} e^{i[k_P(z\sin\theta_P + x\cos\theta_P - c_P t)]} \\ \boldsymbol{u_{SV}} &= \boldsymbol{A_{SV}} e^{i[k_{SV}(z\sin\theta_{SV} + x\cos\theta_{SV} - c_{SV} t)]} \end{aligned}, \tag{1}$$

where $\boldsymbol{A}$ is the polarization vector; k is the wavenumber; θ is the incident angle; c is the wave velocity; the subscripts P or SV represent for the P- or SV-wave, respectively. After the incident wave passes through the metasurface, the wave mode transformation will occur. Then the wave fields in medium B of the transmitted P- and SV-waves can be expressed as

$$\begin{aligned} \boldsymbol{u'_P} &= \boldsymbol{A'_P} e^{i[k'_P(z\sin\theta'_P + x\cos\theta'_P - c'_P t) + \Delta\phi_P]} \\ \boldsymbol{u'_{SV}} &= \boldsymbol{A'_{SV}} e^{i[k'_{SV}(z\sin\theta'_{SV} + x\cos\theta'_{SV} - c'_{SV} t) + \Delta\phi_{SV}]} \end{aligned}, \tag{2}$$

where the superscript " ′ " means the variables for the transmitted waves.

Taking the P-wave incidence as an example, according to the continuous conditions at the interface (i.e., $x = 0$), we can get

$$k_P(z\sin\theta_P - c_P t) = k'_P(z\sin\theta'_P - c'_P t) + \Delta\phi_P = k'_{SV}(z\sin\theta'_{SV} - c'_{SV} t) + \Delta\phi_{SV}. \tag{3}$$

Considering $k_P c_P = k'_P c'_P = k'_{SV} c'_{SV} = \omega$ with ω being the angular frequency, we can obtain the following relations:

$$k_P z\sin\theta_P = k'_P z\sin\theta'_P + \Delta\phi_P = k'_{SV} z\sin\theta'_{SV} + \Delta\phi_{SV}. \tag{4}$$

Taking the derivation w.r.t z on both sides of Eq. (4), we can get the generalized Snell's law for the P-wave incidence

$$k_P\sin\theta_P = k'_P\sin\theta'_P + \frac{\mathrm{d}\Delta\phi_P}{\mathrm{d}z} = k'_{SV}\sin\theta'_{SV} + \frac{\mathrm{d}\Delta\phi_{SV}}{\mathrm{d}z}. \tag{5}$$

Similarly, the generalized Snell's law for the SV-wave incidence can be obtained as:

$$k_{SV}\sin\theta_{SV} = k'_P\sin\theta'_P + \frac{\mathrm{d}\Delta\phi_P}{\mathrm{d}z} = k'_{SV}\sin\theta'_{SV} + \frac{\mathrm{d}\Delta\phi_{SV}}{\mathrm{d}z}. \tag{6}$$

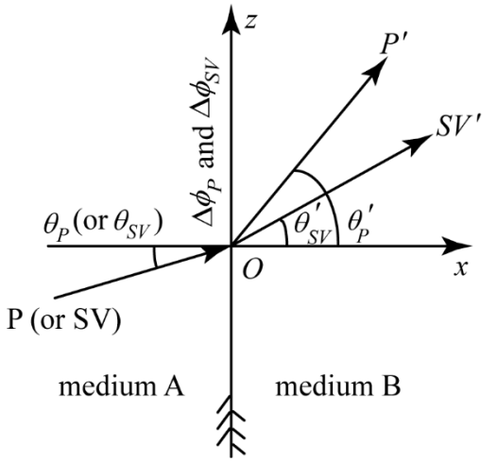

Fig. 1 Schematic illustration of the GSL for the transmitted waves of the mixed in-plane modes.

From Eq. (5) or (6) we can see that if the relation between $\mathrm{d}\Delta\phi_P/\mathrm{d}z$ and $\mathrm{d}\Delta\phi_{SV}/\mathrm{d}z$ is known, then the transmission directions for the P- and SV-waves can be determined directly. Next, we will derive the relation between $\mathrm{d}\Delta\phi_P/\mathrm{d}z$ and $\mathrm{d}\Delta\phi_{SV}/\mathrm{d}z$.

The phase difference between the refracted P-wave (ϕ_P) and SV-wave (ϕ_{SV}) at any point (x, z) with $x \geq 0$ is:

$$\phi_P - \phi_{SV} = [k'_P(z\sin\theta'_P + x\cos\theta'_P - c'_P t) + \Delta\phi_P] - [k'_{SV}(z\sin\theta'_{SV} + x\cos\theta'_{SV} - c'_{SV} t) + \Delta\phi_{SV}]. \tag{7}$$

Substituting Eq. (4) into Eq. (7), we can obtain

$$\phi_P - \phi_{SV} = k'_P x\cos\theta'_P - k'_{SV} x\cos\theta'_{SV} = x(k'_P\cos\theta'_P - k'_{SV}\cos\theta'_{SV}), \tag{8}$$

which implies that $\phi_P - \phi_{SV}$ at an arbitrary point ($x \geq 0$) is independent of the variable z, i.e.

$$\frac{\partial}{\partial z}(\phi_P - \phi_{SV}) = 0 \cdot \tag{9}$$

Eq. (9) holds in the whole transmision region ($x \geq 0$). Considering the fact that the phase difference between P- and SV-waves ($\phi_P - \phi_{SV}$) is equal to $\Delta\phi_P - \Delta\phi_{SV}$ at the side of the metasurface facing the transmission region (i.e. $x \to 0^+$), we obtain, from Eq. (9),

$$\frac{\mathrm{d}\Delta\phi_P}{\mathrm{d}z} = \frac{\mathrm{d}\Delta\phi_{SV}}{\mathrm{d}z}, \tag{10}$$

Substituting Eq. (10) into Eq. (5) or Eq. (6), we can get

$$k'_P \sin\theta'_P = k'_{SV} \sin\theta'_{SV}, \tag{11}$$

i.e.,

$$\frac{\sin\theta'_P}{\sin\theta'_{SV}} = \frac{k'_{SV}}{k'_P} = \frac{c'_P}{c'_{SV}}. \tag{12}$$

The above formula shows that the relations between the refraction directions of the P- and SV-waves are the same as the classical Snell's law and are independent of the incident wave. Eq. (12) also shows that the refraction angle of the P-wave is greater than that of the SV-wave. Therefore, when the refraction angle of the P-wave $\theta'_P = 90°$, we have a critical refraction angle of the SV-wave $\theta'_{SV0} = \sin^{-1}(c'_{SV} / c'_P)$ beyond which the refracted P-wave becomes evanescent.

Eqs. (5), (6) and (12) can be applied to design elastic metasurfaces for wave front modulation. If one steers an incident P (or SV) wave, Eq. (5) [or (6)] should be used; and the propogation direction of the SV (or P) wave can be determined by Eq. (12).

3. The metasurface and tunable functional units

According to the above GSL for the mixed in-plane wave modes, the metasurface can be designed to manipulate the transmitted in-plane waves. First, the functional unit providing 2π phase shift should be designed. As shown in Fig. 2, the functional unit with the finite element mesh as designed in Ref. [45] is used to manipulate the in-plane wave mode. The values of the geometric parameters are shown in Table I. It can be seen that the shape of the functional unit (Fig. 2(a)) looks like a fish-bone with 6 pairs of screw bolts (bones) of equal length and two symmetrical rows of nuts as vibrators, so the metasurface is named as a "fish-bone metasurface". As we know that the position of the nut on each screw-bolt can be adjusted by screwing in or out according to the screw-and-nut mechanism, then the phase shift and transmittance of the transmitted wave can be tuned continuously. The orange and green regions represent the host (aluminum) and vibrators (steel), respectively. The material parameters of the aluminum are: mass density ρ = 2700kg/m^3, longitudinal wave velocity c_P = 5351m/s and shear wave velocity c_{SV} = 3097m/s, and those of the steel are: ρ = 7670kg/m^3, c_P = 6010m/s and c_{SV} = 3150m/s.

It should be noticed that for the manipulation of the refracted waves, not only the phase shift but also the efficiency of the functional unit needs to be guaranteed at the same time. Then the phase shift and the transmittance of the functional unit varying with the screw-in depths (s) are calculated by using the finite element software COMSOL Multiphysics 5.3. A line source with in-plane

excitation is set on the left side far from the "fish-bone" structure to generate a stable incident wave. The excitations along the *x*-axis and *z*-axis simulate the P- and SV-waves, respectively. Perfectly matched layers (PMLs) are used on both ends of the functional unit to avoid any reflection from the boundaries. Continuous periodic boundary conditions are applied to the upper and lower boundaries of the functional unit, as shown in Fig.2(a). The phase shift and the transmittance are obtained by taking the averaged displacements along a line (detection line) in the far area of the right side [42].

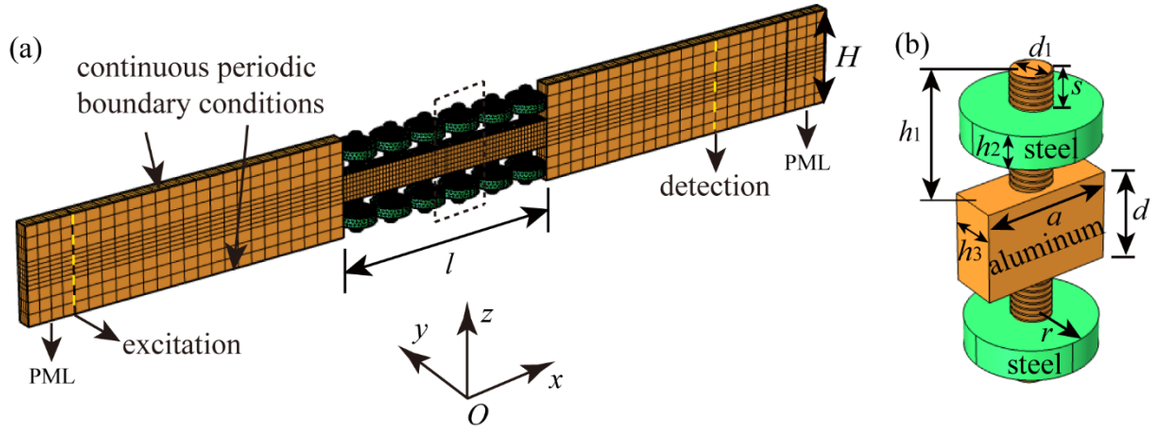

Fig. 2 Schematic diagrams of the functional unit (a) and basic element (b).

Table I. Geometric parameters (unit: mm).

l	H	h_1	h_2	h_3	d	d_1	r	$a = l/6$
48	20	7.1	2	3	5.6	2.4	3.9	8

As stated above, the phase shift and transmittance properties for P- or SV-waves can be calculated in the case of the P- or SV-wave incidence, and are illustrated in Figs. 3 and 4, respectively. The transmittances of P-wave (ξ_P) and SV-wave (ξ_{SV}) are defined as

$$\xi_P = \frac{A_P}{A_{P0}} \quad \text{and} \quad \xi_{SV} = \frac{A_{SV}}{A_{SV0}}, \tag{13}$$

where A_P and A_{SV} are the transmitted displacement amplitudes of P- and SV-waves for the functional unit, respectively; and A_{P0} and A_{SV0} are those for the uniform structure without the fish-bone structure.

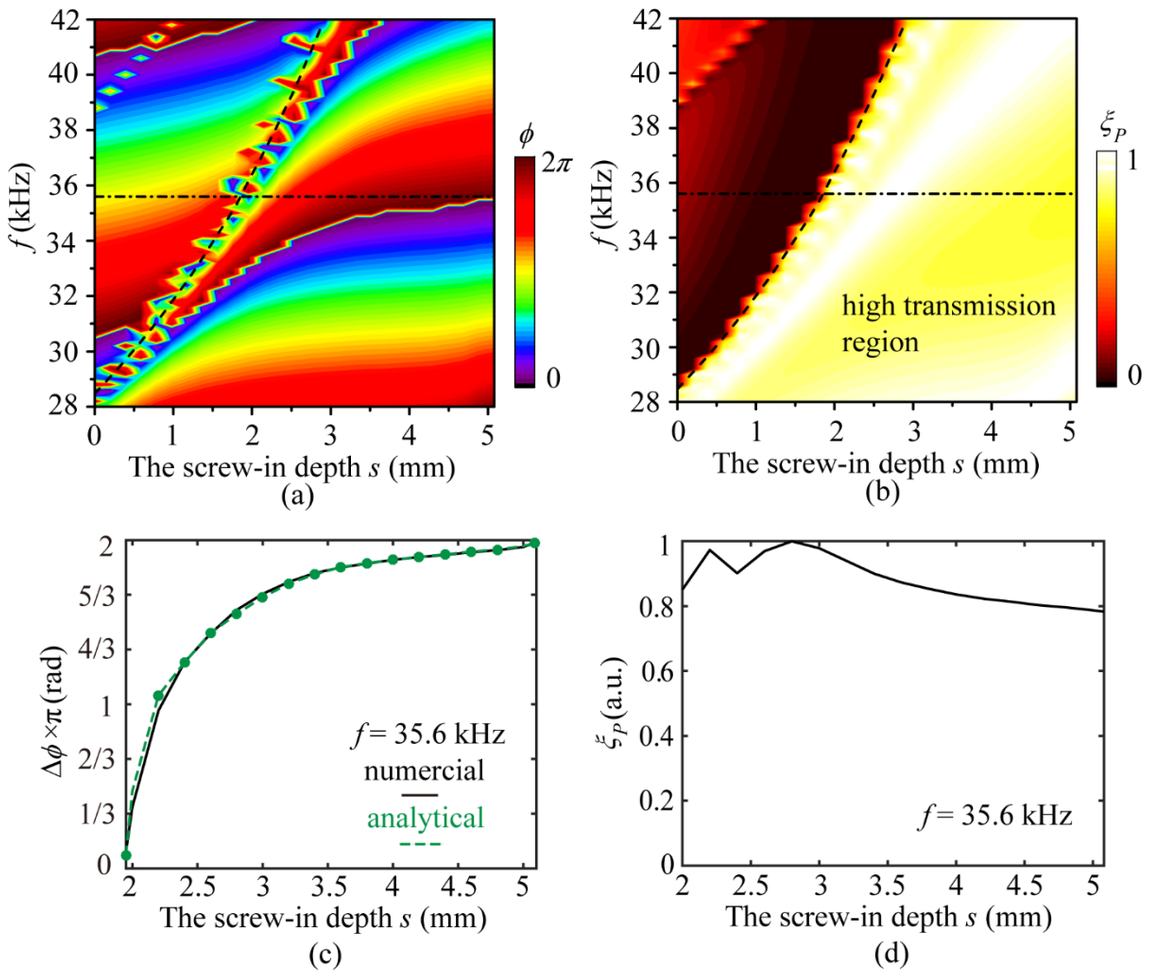

Fig. 3 The phase shift and transmittance of the transmitted P-wave. The nephograms of phase shift (a) and transmittance (b) varying with the screw-in depth and frequency for the functional unit; (c) the phase shifts obtained by numerical simulation (the black solid curve) and analytical calculation (the green dashed curve) at f = 35.6 kHz; (d) the transmittance obtained by numerical simulation at f = 35.6 kHz.

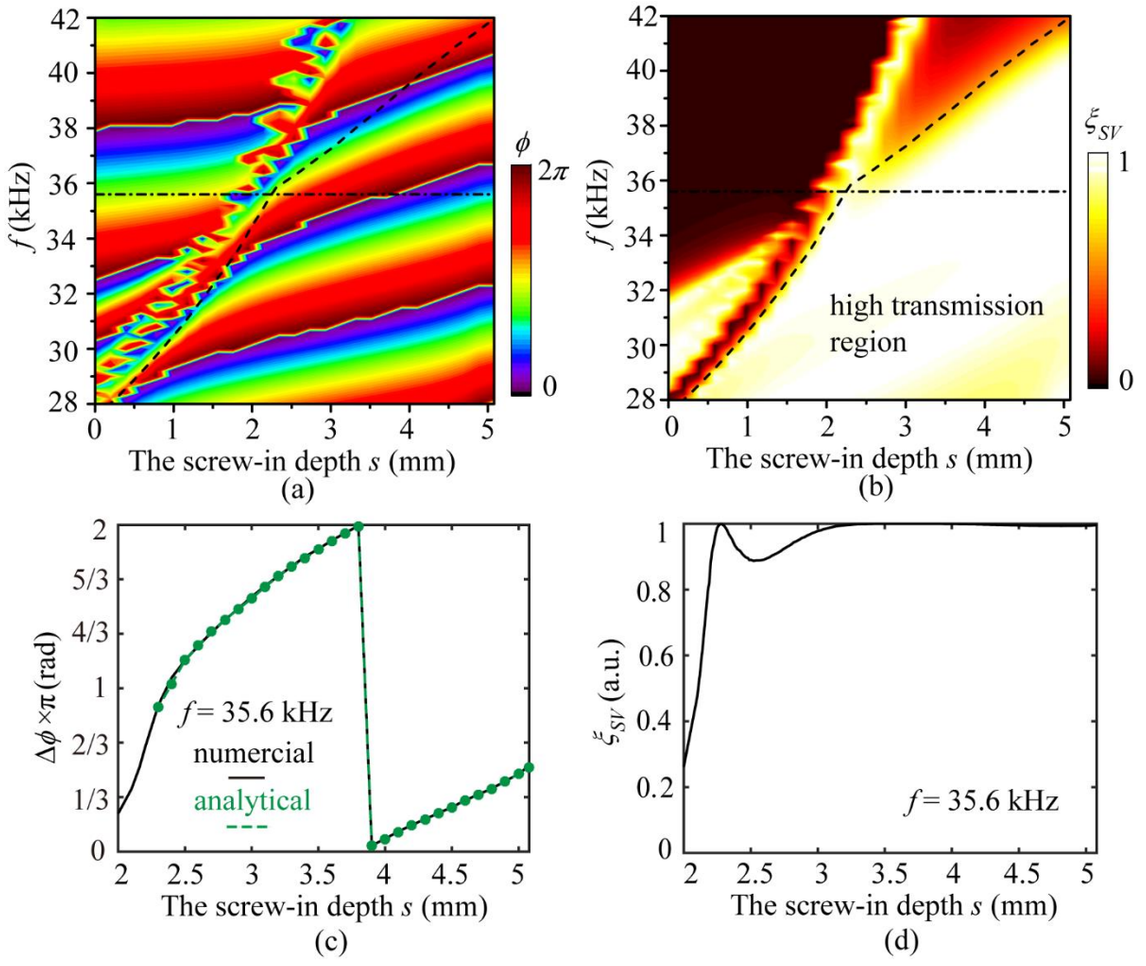

Fig. 4 The phase shift and transmittance of the transmitted SV-wave. The nephograms of phase shift (a) and transmittance (b) varying with the screw-in depth and frequency for the functional unit; (c) the phase shifts obtained by numerical simulation (the black solid curve) and analytical calculation (the green dashed curve) at f = 35.6 kHz; (d) the transmittance obtained by numerical simulation at f = 35.6 kHz.

From the nephograms of the phase shift for the transmitted P- and SV-waves, as shown in Figs. 3(a) and 4(a), it can be found that the phase shift indeed has a full 2π coverage in a wide frequency range (28 – 42 kHz). The corresponding wavelengths for the P- and SV-waves are 191 – 127 mm and 111 – 74 mm, respectively. The thickness of the metasurface (l = 48 mm) is less than the wavelength. The transmittance is higher than 70% below the oblique dashed line, but is very low above this line, see Figs. 3(b) and 4(b). Therefore, the high transmission regions below the oblique lines will be considered in the following design. As an illustration, the phase shift curves for a particular frequency of f = 35.6 kHz are plotted in Figs. 3(c) and 4(c) by the black solid curves which are obtained directly by sectioning, respectively, Figs. 3(a) and 4(a) along the dot-dashed line. And the corresponding curves of the normalized transmittance are depicted in Figs. 3(d) and 4(d). It is clearly seen that the phase shift covers a full 2π span and the transmittance is generally higher than 70%.

3.2 Mechanism of phase-shift tunability

When the wave propagates through the "fish-bone" functional unit, the phase shift can be obtained by

$$\phi = 2\pi\, fl/c_{\text{phase}}\,, \tag{14}$$

where $c_{\text{phase}} = 2\pi f/k$ is the phase velocity with k being the wave number. For a given frequency, c_{phase} can be calculated from the dispersion curves of the infinite 1D periodic structure in which the basic element is the unit cell, as shown in Fig. 5(a). For different screw-in depths of the nuts, the dispersion curve can be calculated by using the finite element method together with the Bloch theorem. The results in the first Brillouin zone of the 1D periodic structures with the screw-in depth being 1.7, 3.0, and 4.5 mm are shown in Fig. 5(b)-(f). The color scale represents the value of

$$\eta_i = \frac{\left|\int_V u_i \mathrm{d}V\right|}{\left|\int_V \sqrt{u_x^2 + u_y^2 + u_z^2}\,\mathrm{d}V\right|}, \tag{15}$$

where i represents for x, y and z; u_x, u_y and u_z are the displacement components in x, y, and z directions, respectively; and the integrals are taken over the volume (V) of one basic element. As shown in Figs. 5(b), (c) and (e), $\eta_i \to 1$ (the dark red color) represents for the u_i -dominated wave mode, i.e., $\eta_y \to 1$, $\eta_x \to 1$ and $\eta_z \to 1$ means the flexural-, P- and SV-dominated wave modes, respectively. This also can be tested by the vibrational modes. Here, in the case of f = 35.6 kHz, Figs. 5(d) and (f) show the vibrational modes of points 1, 2 and 3, 4 which are the vibrational modes of the P- and SV- dominated wave modes, respectively. It should be noticed that for the flexure-dominated wave studied in Ref. [45], the operating frequency zone is 7 – 13 kHz. However, for the in-plane waves, the operating frequency zone should be as high as 28 – 42 kHz to ensure that the phase shifts of P- and SV-waves cover 0-2π simultaneously. Bands a and b are considered for P- and SV-dominated waves as shown in Figs. 5(c) and (e), respectively. The phase velocity can be calculated easily from the crosspoints on the dispersion bands. The phase velocity curves of the P- and SV-wave modes varying with s at f = 35.6 kHz are illustrated in Figs. 6(a) and (b), respectively. Then according to Fig. 6 and Eq. (14), the phase shifts can be obtained which are illustrated in Figs. 3(c) and 4(c) by the green dashed curve. It is consistent with the black solid curve obtained by numerical simulation. It is also found that the black dot-dashed lines (f = 35.6 kHz) have no crosspoint with the dispersion curve a or b for s = 1.7 mm, meaning that f = 35.6 kHz locates in the bandgap of the P- or SV-wave mode, which explains why in this case the transmissions are very low as shown in Figs. 3(b) and 4(b).

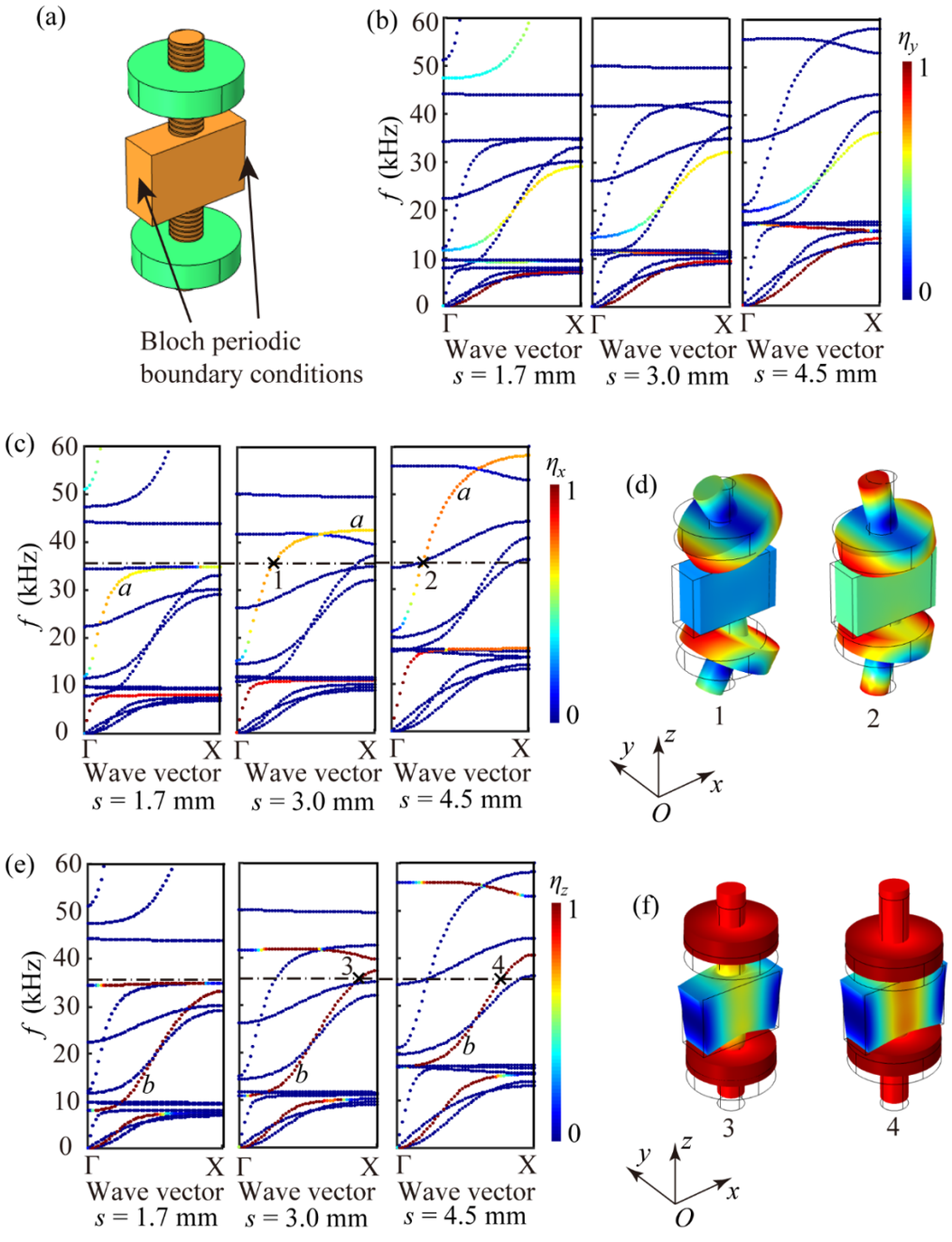

Fig. 5 (a) The unit with Bloch periodic boundary conditions to calculate the dispersion curves; (b), (c) and (e) the dispersion curves of the above unit for the screw-in depth s = 1.7, 3.0 and 4.5 mm; (d) the P-dominated wave modes and (f) the SV-dominated wave modes corresponding to crosspoints "x" at f = 35.6 kHz for s = 3.0 and 4.5 mm.

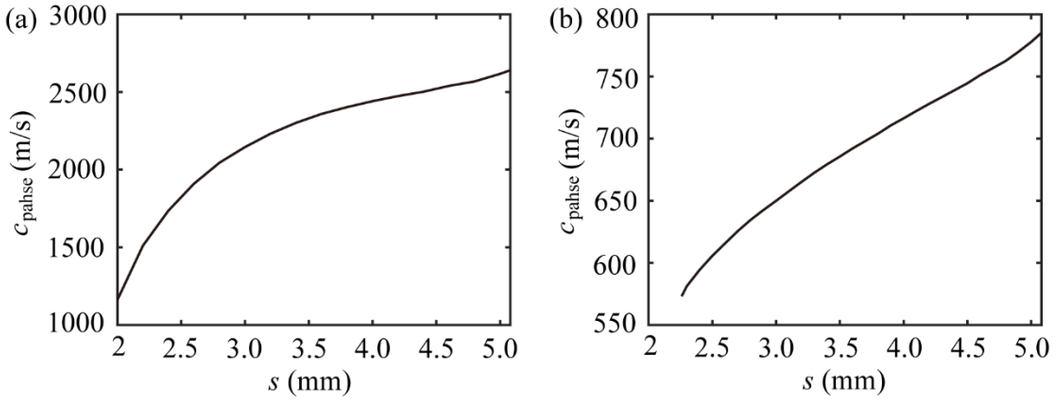

Fig. 6 The phase velocities varying with the screw-in depth at the frequency f = 35.6 kHz of the transmitted P (a) and SV (b) waves, respectively.

4. Design of the metasurface for manipulating P- and SV-waves simultaneously

In this section, we will design the metasurfaces based on the GSL for the mixed in-plane waves and the nephograms of phase shift and transmittance to realize the manipulation of the transmitted P- and SV-waves. The calculation model in a front view (xz-plane) is shown in Fig. 7. The boundaries aroud the model are set as PMLs. A surface traction along the x- or z-direction with the amplitude of $\left[1\cdot\exp(-(z-\alpha H)^2/w_0^{\,2})\right]$ (N/m^2) is applied at the yellow dashed line to excite a Gaussian beam of the P- or SV-wave mode. Multi-functions such as directional refraction (α = 16.5 and $w_0 = 30H$) and wave focusing (α = 0 and $w_0 = 40H$) will be realized numerically.

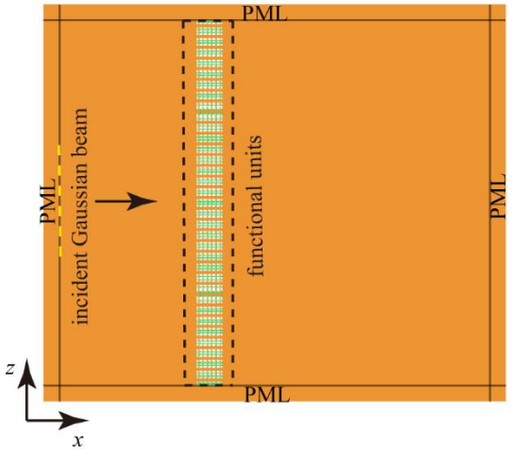

Fig. 7 The model of the metasurface constructed in COMSOL Multiphysics.

4.1 Directional refraction

For the transmitted wave propagating along the designated direction, the required phase shift of each functional unit can be calculated from Eq. (5) and Eq. (6). Once the phase shifts are known, we can obtain the corresponding screw-in depths from Figs. 3(a) and 4(a). Then the metasurface with the function of directional refraction can be obtained.

a. Normal incidence of P-wave

First, we consider the normal incidence of a P-wave and design the metasurface based on Fig. 3(a) to control the refraction angle of the P-wave being 30° with f = 31.4 kHz. The phase shift curves of the P-wave in Fig. 3(a) are used to determine the screw-in depths of every functional unit of the metasurface (refer to Appendix A for the detailed values). Figs. 8(a) and (c) are the divergence and curl of displacement fields, respectively, which represent the P- and SV-wave fields; the corresponding polar directivity graphs of the transmitted waves measured at far fields are presented in Figs. 8(b) and (d). We can see that the metasurface can steer the P-wave nearly in the designed direction (red dot-dashed line). Due to the limited width of the incident beam and the influence of the near-field scattering, there is a little deviation between the numerically estimated direction (yellow arrow) and the desired direction (red dot-dashed line). And at the same time, the refraction angle of the SV-wave calculated by Eq. (12) is 17°; the estimated refraction angle by the curl of displacement fields is close to this value. Then, with the same target of the regulation (i.e. the refraction angle of the P-wave is 30°), the metasurface is tuned for a different operating frequency f = 35.6 kHz (the screw-in depths are presented in Appendix A). The numerical results for the divergence (P-wave) and curl (SV-wave) of displacement fields are shown in Figs. 8(e) and (g), respectively, with the corresponding polar directivity graphs shown in Figs. 8(f) and (h). It can be seen that the refraction direction is independent of the incident wave frequencies. The results verify the correctness of Eq. (12), i.e., for the mixed in-plane mode, if the propagation direction of one wave mode in the transmitted medium is decided, the direction of another wave mode is then determined. In other words, the transmitted P- and SV-waves are related by Eq. (12).

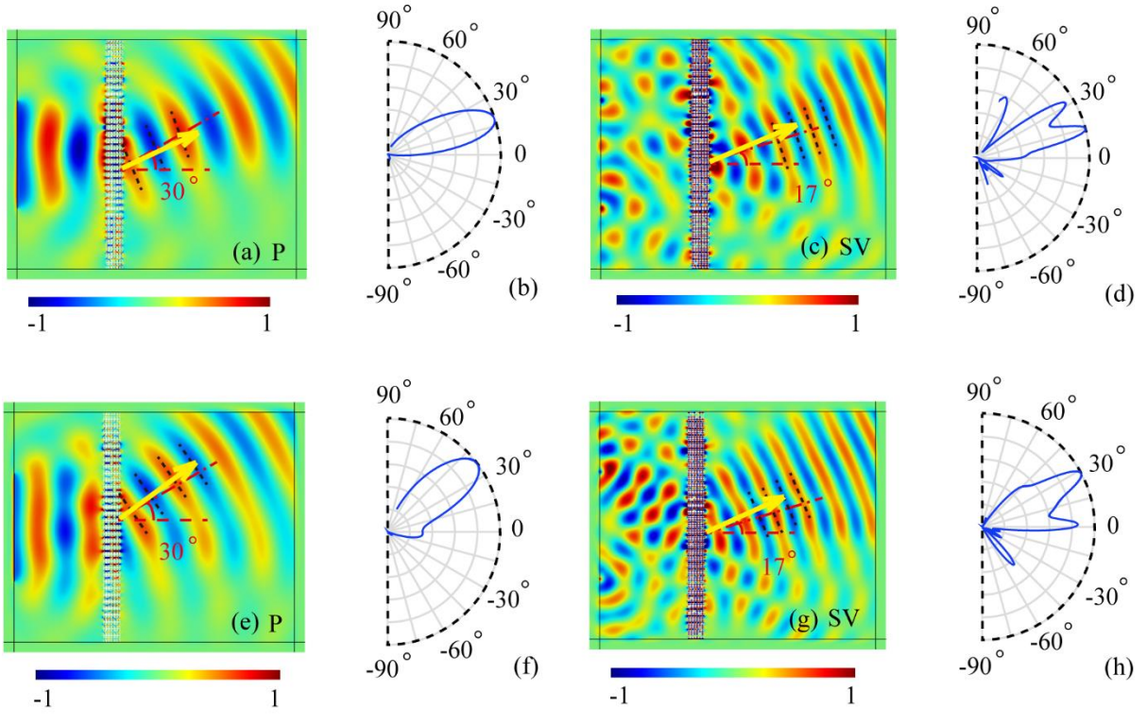

Fig. 8 Normalized divergence (a, e) and curl (c, g) of the displacement fields for the normal incidence of a P-wave with frequencies f = 31.4 kHz (a, c) and 35.6 kHz (e, g). The designed refraction angle of the refracted P-wave is 30°. The polar directivity graphs (b, d, f and h) of the transmitted waves measured at far fields correspond to the numerical simulation results (a, c, e and g), respectively.

Next, we try to steering the refracted P-wave in the direction of 90°. What we need to do is to

tune the screw-in depth (shown in Appendix A) of every functional unit of the same metasurface to get the phase shift we need. In this case, the numerical results of the divergence and curl of displacement fields are illustrated in Figs. 9(a) and (b), respectively. It can be seen that the refracted P-wave propagates approximately along the desired direction (red dotted line) as shown in Fig. 9(a). If the refraction angle is large, the wave front is slight curved under the influence of the near-field scattering. In addition, it is noted that the incident beam has a limited width, so the propagating-to-evanescence transformation is only effective within the beam width. The transmitted wave will spread out outside the beam width, especially when the target transmission angle is 90°. Therefore, it's very difficult to realize perfect grazing. Fig. 9(b) shows that the refracted angle of the SV-wave is also close to 35° which is calculated by Eq. (12) (red dot-dashed line). Generally speaking, these results show that the metasurface can steer the refracted P-wave to propagate in the targeted direction with the refraction angle of the SV-wave determined by Eq. (12).

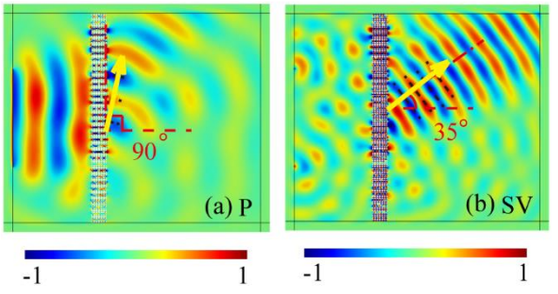

Fig. 9 Normalized divergence (a) and curl (b) of the displacement fields for the normal incidence of a P-wave with frequency f = 35.6 kHz. The designed refraction angles of the P-wave is 90°.

Eq. (12), which is derived from Eq. (10), is verified by the above numerical simulation. Next we will check Eq. (10) directly through comparision of $\Delta\phi_P$ and $\Delta\phi_{SV}$. Fig. 10 shows the phase shifts of every functional unit when the refraction angle of the P-wave is 30° with f = 35.6 kHz. The phase shift of the P-wave (blue dots) for each functional unit is calculated from the first two items of Eq. (5). Then the screw-in depths of every functional unit can be obtained from the linear interpolation in Fig. 3(a). The phase shift of the SV-wave (red rhombuses) corresponding to these screw-in depths can be obtained from Fig. 4(a) directly. We can see from Fig. 10 that the slopes of the two results are approximately equal, which verifies the reliability of Eq. (10).

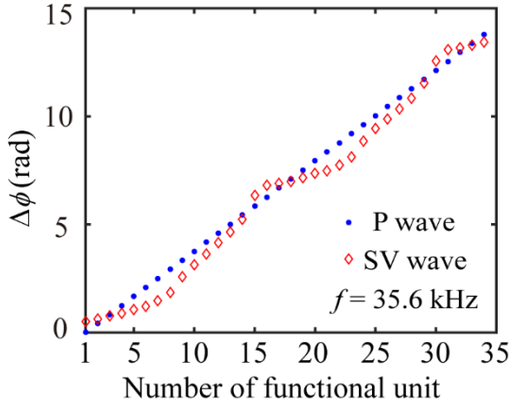

Fig. 10 Phase shifts for every functional unit of the metasurface to control the refraction angle of P-wave is 30° at 35.6 kHz.

b. Normal incidence of SV-wave

In the above section, the steering of the P-wave is discussed for the P-wave incidence. In this section, the normal incidence of an SV-wave will be considered. Steering of both P- and SV-waves will be examined based on the phase shift curves of SV-wave (Fig. 4). We first consider the steering of the refracted P-wave in the angle of 30° for f = 35.6 kHz. In this case, the refraction angle of the SV-wave can be obtained by Eq. (12), which is 17° (red dot-dashed line). Then the phase shift curves of SV-wave (Fig. 4) are used to obtain the phase shifts and the screw-in depth of every functional unit to design the metasurface. The numerical results are shown in Fig. 11, in which (a) is the divergence of displacement field and (c) is the curl of displacement field. Figs. 11(b) and (d) are the corresponding polar directivity graphs. It is seen that our target is largely achieved, i.e., the refracted P-wave propagates at 30° with the SV-wave refracted at 17°. If the refracted P-wave is steered in the direction along the metasurface ($\theta'_p = 90°$), the refraction angle of SV-wave should be θ'_{sv0}=35° based on Eq. (12). The numerical simulations are shown in Figs. 11(e) and (g) with the corresponding polar directivity graphs shown in Figs. 11(f) and (h). The evanescent behavior of the refracted P-wave is seen clearly. There are three refracted beams (yellow arrows) appearing in the transmitted field in Fig. 11(g). One is the refracted SV-wave as expected, which propagates in the theoretical direction of 35° obtained by Eq. (12) (red dot-dashed line). And the remaining two beams are the leaked waves caused by higher-order diffraction [46]. It can be seen that the three directions shown in the polar directivity graph Fig. 11(h) agree with those in Fig. 11(g). The appearance of these undesired waves indicates that our design is not perfect yet and should be optimized. However, the optimization of a tunable metasurface is a challenging problem and deserves further research.

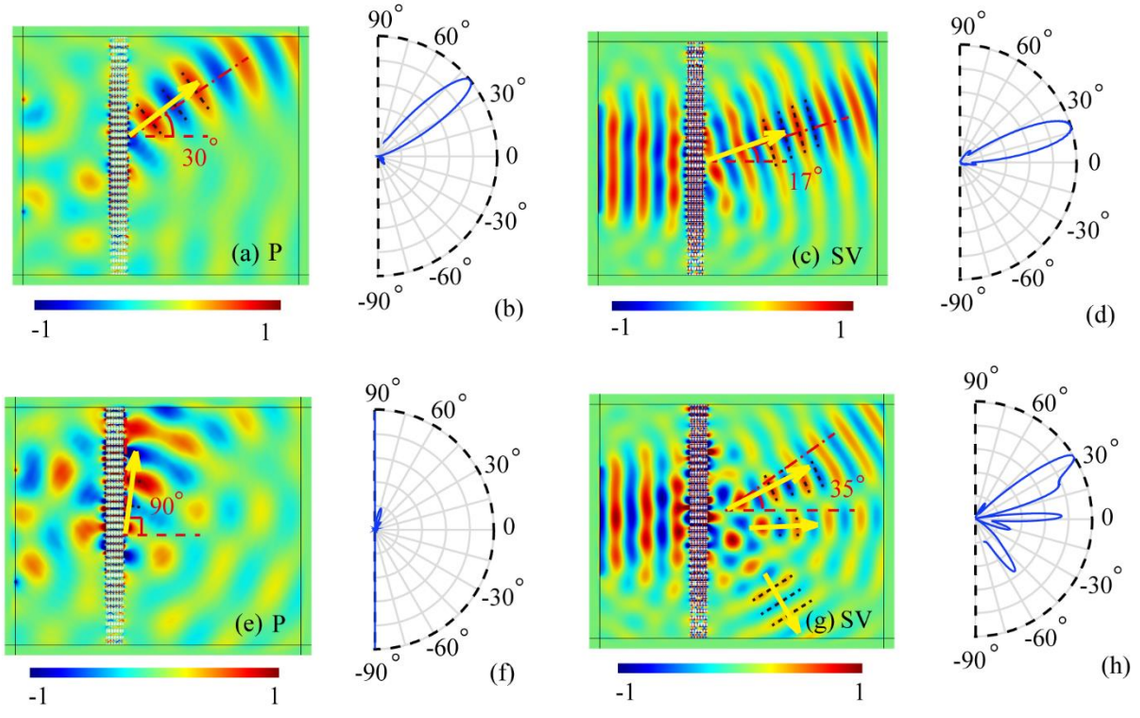

Fig. 11 Normalized divergence (a, e) and curl (c, g) of displacement fields for the normal incidence of SV-wave at 35.6 kHz. The desired refraction angles of P-wave are 30° (a) and 90° (e), and the refraction angles of SV-wave obtained from Eq. (12) are 17° (c) and 35° (g), respectively. The polar directivity graphs (b, d, f and h) of the transmitted waves measured at far fields correspond to the numerical simulation results (a, c, e and g), respectively.

It was indicated previousely that when the refraction angle of the SV-wave is bigger than the critical value θ'_{SV0}, the refracted P-wave will becomes evanescent. For example, if we target the refraction angle of the SV-wave at 60° which is bigger than θ'_{SV0}=35°, the refracted wave P-wave is observed to be transferred into the evanescent wave, see Figs. 12(a) and (b). When the refracted SV-wave is steered along the surface (i.e. $\theta'_{SV} = 90°$), all transmission waves become evanescent, see Figs. 12(c) and (d). For the same reason as we explained before, the simulated directions (yellow arrows) deviate a bit from the desired directions (red dot-dashed lines), as shown in Figs. 12(a) and (c). In Fig. 12(d), the downstream wave is the leaked wave, similar to the situation in Fig. 11(g). In thses two cases, the metasurfaces are designed based on the phase shift curves of SV-wave in Fig. 4. The detailed values of the screw-in depths of the functional units are presented in Appendix A.

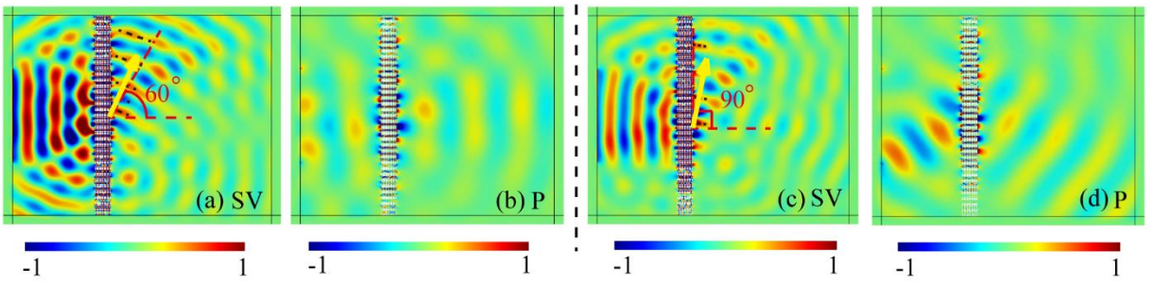

Fig. 12 Normalized curl (a, c) and divergence (b, d) of displacement fields for the normal incidence of SV-wave at 35.6 kHz. The manipulation targets are (a, b) the refraction angle of SV-wave is 60°, and P-wave is transfered into evanescent wave; (c, d) The transmitted SV-wave is steered along the metasurface, and P-wave has aleardy become evanescent wave.

c. Oblique incidence of SV-wave

Consider the oblique incidence of the SV-wave at 15° with the operating frequency of 35.6 kHz. The targeted refraction angle of the SV-wave is 30° or 60° (red dot-dashed line). The results are shown in Fig. 13 which demonstrate the efficiency of the designed metasurface (the detailed screw-in depths of the units are listed in Appendix A). For the 30° refraction of the SV-wave, the P-wave propagates at the angle of 60° which is close to the value calculated from Eq. (12) (red dot-dashed line). Fig. 13(d) shows that the refracted P-wave becomes evanescent when the targeted refraction angle of the SV-wave is 60° which is larger than θ'_{SV0}.

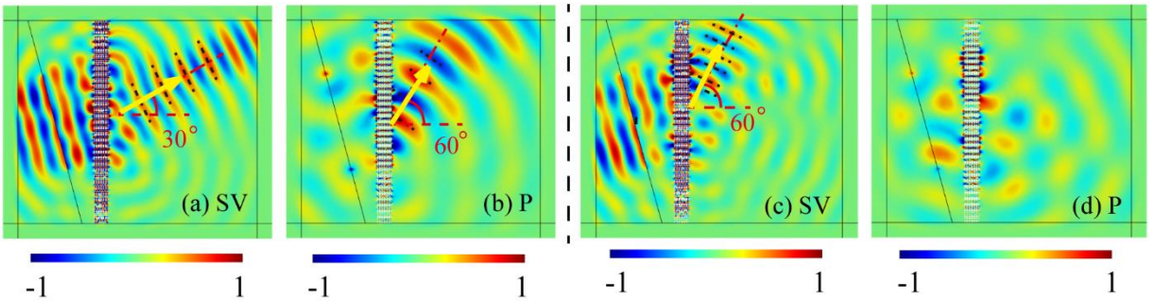

Fig. 13 Normalized curl (a, c) and divergence (b, d) of displacement fields for the obliquely incident SV-wave of 35.6 kHz with the incident angle of 15°. Steer the SV-wave at 30° (a) with the refraction angle of the P-wave being 60° (b); Steer the SV-wave at 60° (c) with the P-wave becoming evanescent (d).

4.2 Wave focusing

In this part, we design metasurface to realize the focusing of the refracted P-wave. The central focusing and arbitrary point focusing are considered. For the central focusing, the schematic diagram is illustrated in Fig. 14. The red dashed lines represent the P-wave, and the black solid lines represent the SV-wave. We suppose that the P-wave is focused at point O_1 (x, 16.5H). Then according to the GSL, the required phase shift of each functional unit can be determined by [44]:

$$\phi_n - \phi_1 = \frac{2\pi}{\lambda}\left(\sqrt{(z_n - 16.5H)^2 + x^2} - \sqrt{(z_1 - 16.5H)^2 + x^2}\right), \tag{16}$$

where n is the serial number of the functional unit. It should be noticed that the metasurface should be symmetric about z = 16.5H for the central focusing, so we can just calculate the phase shifts of half the functional units (e.g., n = 2-17) as shown in Fig. 14. By combining Fig. 3(a), the screw-in depth for each functional unit of the metasurface can be obtained to realize the focusing of the refracted P-wave.

Then what happens to the refracted SV-wave? According to Eq. (12), the behavior of the SV-wave can be estimated as shown in Fig. 14. Assume that for the nth functional unit the refraction angle of the P-wave is θ'_{Pn}, and that of the SV-wave is θ'_{SVn}. Then

$$\tan\theta'_{Pn} = \frac{16.5H - (n-1)H}{x}. \tag{17}$$

From Eq. (12), we can get

$$\sin\theta'_{SVn} = \frac{c'_{SV}\sin\theta'_{Pn}}{c'_P}. \tag{18}$$

As shown in Fig. 14, the coordinate of the crosspoint O_2 (x', 16.5H) of the SV-wave beams and the central axis (z = 16.5H) can be determined as

$$x' = \frac{16.5H - (n-1)H}{\tan\theta'_{SVn}}. \tag{19}$$

Table II illustrates the values of x' when the P-wave with the operating frequency f = 35.6 kHz focusing on O_1 (x, 16.5H) = (150 mm, 330 mm). In this case, the results are shown in Fig. 14. For the sake of clearance, we have omitted some beams. As shown in Fig. 14, all the beams will pass through the wedge ABC. The wave beams near AB and AC are relatively dense, indicating that the energy near lines AB and AC is relatively concentrated. The corresponding numerical results

computed by Comsol Multiphysics are shown in Fig. 15. We can see that the P-wave indeed focuses on the targeted position, O_1, as shown in Fig. 15(b). And the size and position of the focus area of the SV-wave shown in Fig. 15(c) are approximately the same as the analytical results. If the operating frequency changes, the metasurface still works just by tuning the screw-in depths of the functional units. Figs. 15(d), (e) and (f) show the focusing results for another choice of frequency, f = 31.4 kHz.

Similarly, the focusing of SV-waves can also be realized for the SV-wave incidence. As shown in Fig. 16, when the SV-wave with the frequency of 35.6 kHz is incident, the phase shift and screw-in depth of each functional unit are obtained by the curves of SV-wave (Fig. 4), and then the metasurface is designed to make the SV-wave focus on (250 mm, 330 mm).

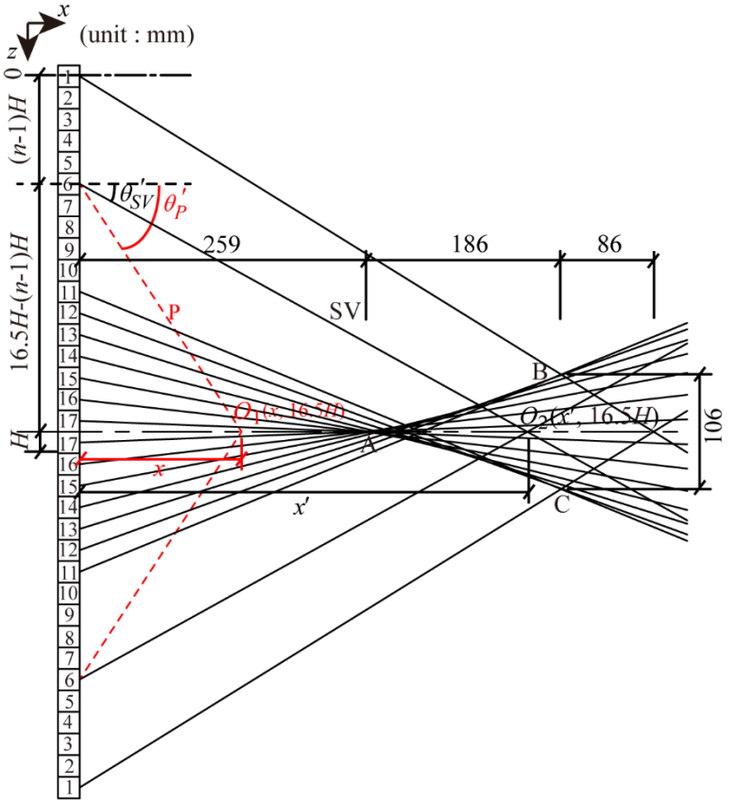

Fig. 14 Schematic diagram of central focusing for the refracted P-wave. The red dashed and black solid lines represent the refracted P- and SV-waves, respectively.

Table II. The intersection points of the SV-wave beams and the center line (z = 16.5H).

n	1	2	3	4	5	6	7	8	9
x' (mm)	260	263	269	277	289	302	317	334	353

n	10	11	12	13	14	15	16	17
x' (mm)	373	393	415	437	460	484	508	532

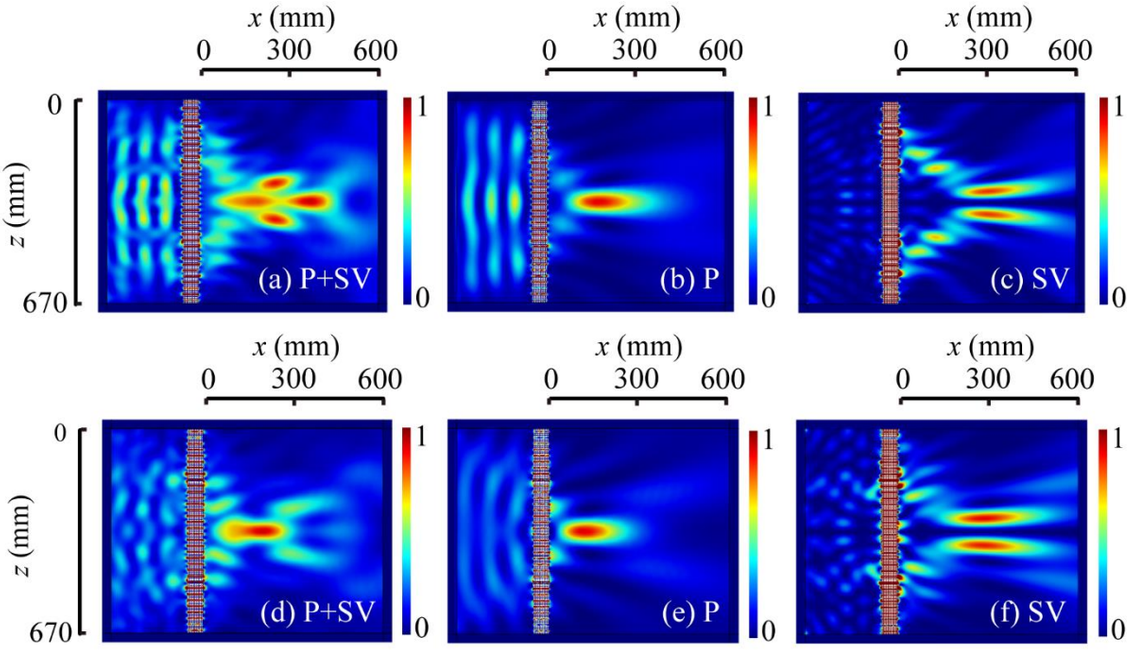

Fig. 15 Results of central focusing for the P-wave incidence with f = 35.6 kHz (a-c) and f = 31.4 kHz (d-f) at O_1(150 mm, 330 mm). (a, d) Normalized total energy fields, (b, e) normalized intensity of divergence of displacement fields, and (c, f) normalized intensity of curl of displacement fields.

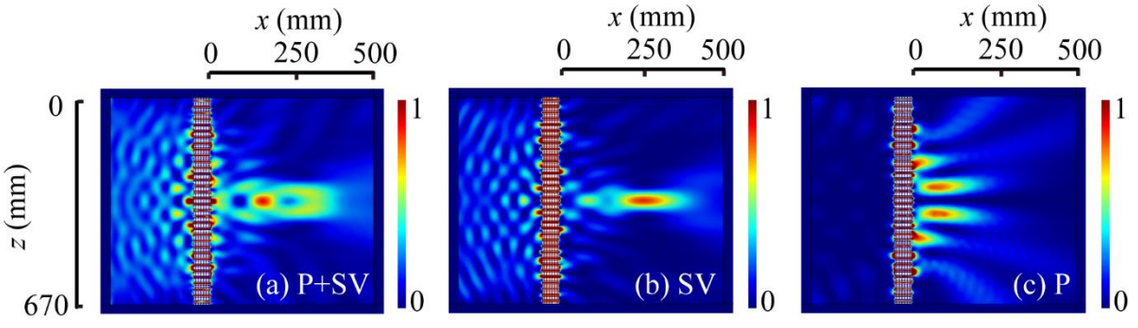

Fig. 16 Results of central focusing for the SV-wave incidence with f = 35.6 kHz at O_1(250 mm, 330 mm). (a) Normalized total energy field, (b) normalized intensity of divergence of displacement field, and (c) normalized intensity of curl of displacement field.

Next the wave focusing at an arbitrary point $O_3(x'', y'')$ for the refracted P-wave will be discussed. In this case, the metasurface is not symmetric. The phase shifts of the functional units can be calculated by [44]:

$$\phi_n - \phi_1 = \frac{2\pi}{\lambda}\left(\sqrt{(z_n - z'')^2 + x''^2} - \sqrt{(z_1 - z'')^2 + x''^2}\right), \tag{20}$$

where n = 2-34. The schematic diagram is shown in Fig. 17. Considering the transmitted wave beam from nth unit, we have

$$\tan\theta'_{Pn} = \frac{(n-1)H - z''}{x''}. \tag{21}$$

According to Eq. (12), we can get

$$\sin\theta'_{SVn} = \frac{c'_{SV}\sin\theta'_{Pn}}{c'_P}. \tag{22}$$

In that way the propagation direction of the SV-wave is determined when the P-wave is focused on (200 mm, 150 mm). On each side of the line EF there are energy dense areas for the SV-wave, as shown in Fig. 17. The simulated results for the P-wave focusing at O_3(200 mm, 150 mm) in case of f = 35.6 kHz and 31.4 kHz are shown in Fig. 18. These results indicate that wave focusing at an arbitrary point can be achieved by the designed metasurface, and there indeed have the energy dense areas for SV-wave as shown in Figs. 18(c) and (f). The numerical simulated results show a good agreement with the analysis. The screw-in depths of all functional units for central focusing and arbitrary point focusing are shown in Appendix A.

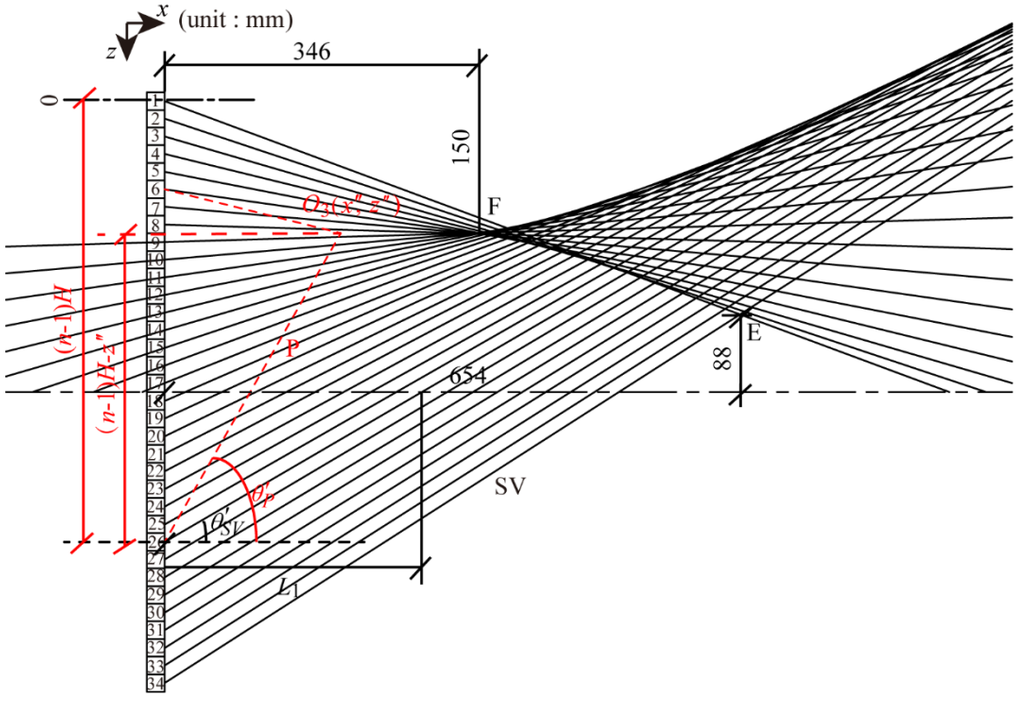

Fig. 17 Schematic diagram of arbitrary point focusing for the refracted P-wave. The red dashed and black solid lines represent the refracted P- and SV-waves, respectively.

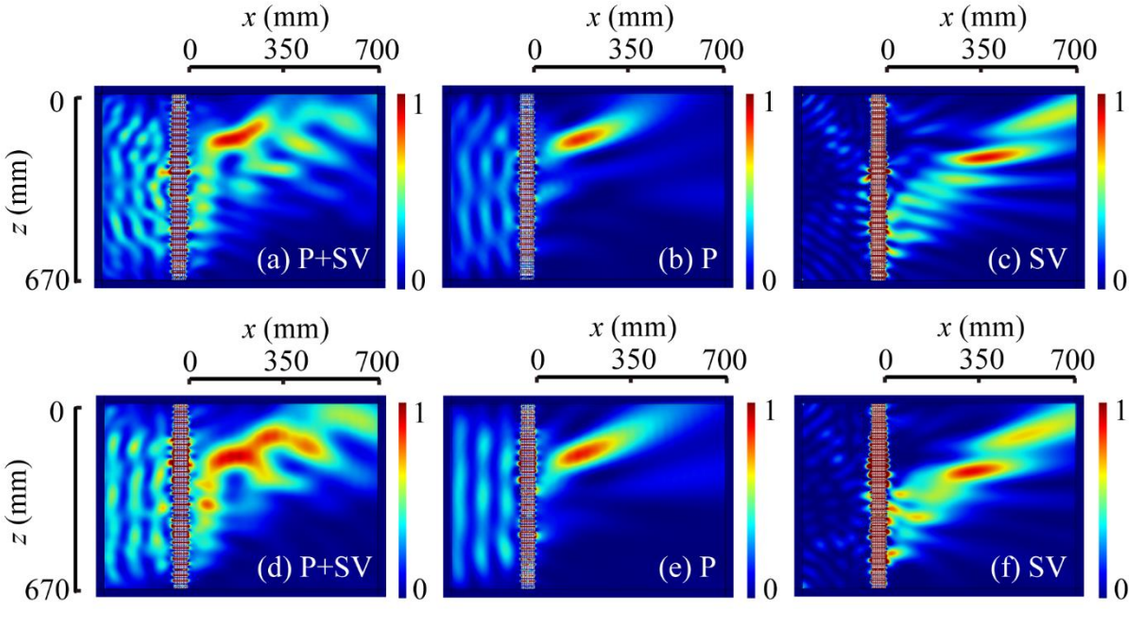

Fig. 18 Results of arbitrary point focusing for the P-wave incidence with f = 35.6 kHz (a-c) and f = 31.4 kHz (d-f) at O_3(200 mm, 150 mm). (a, d) Normalized total energy fields, (b, e)normalized intensity of divergence of

displacement fields, and (c, f) normalized intensity of curl of displacement fields.

5. Conclusions

In this paper, we design a kind of tunable fish-bone elastic metasurface to manipulate transmitted P and SV-waves. We first present the generalized Snell's law for the mixed in-plane wave modes including the relation between the refraction angles of the P- and SV-waves, which allows us to predict another kind of wave's propagation behavior when we regulate one of the waves. The phase shifts of the designed tunable functional unit are obtained numerically and analytically. Then, we design the metasurfaces to achieve directional refraction and focusing for both P- and SV-wave incidence. The distinguishing feature of our design is that the metasurface is continuously tunable and broadband. The present study provides us a way to control mixed in-plane waves.

The present paper only consider the modulation of the transmitted waves. Another interesting topic is the steering of the reflected wave front, especially the simultaneous modulation of refracted and reflected waves which is very challenging.

Acknowledgment

This work was supported by the National Natural Science Foundation of China (Grant Nos. 11872101, 11991031, 11991032, 12021002); the Fundamental Research Funds for the Central Universities (Grant No. 2018JBM032); and the China Scholarship Council (Grant No. 201907090040).

Data Availability

The data that support the findings of this study are available from the corresponding author upon reasonable request.

Appendix A. The screw-in depths of the nuts

The screw-in depths of the nuts to achieve above manipulate targets are given in the following tables. Directional refraction is more complex, so it is summarized in Table III. Tables IV and V show the screw-in depths of the nuts for directional refraction and focusing, respectively.

Table III. Summary of directional refraction.

Case	incidence	Operating frequency	manipulate target
1	Normal incidence of P-wave	31.4 kHz	P-wave → 30°
2	Normal incidence of P-wave	35.6 kHz	P-wave → 30°
3	Normal incidence of P-wave	35.6 kHz	P-wave → 90°
4	Normal incidence of SV-wave	35.6 kHz	P-wave → 30°
5	Normal incidence of SV-wave	35.6 kHz	P-wave → 90°
6	Normal incidence of SV-wave	35.6 kHz	SV-wave → 60°
7	Normal incidence of SV-wave	35.6 kHz	SV-wave → 90°
8	Oblique incidence of SV-wave at 15°	35.6 kHz	SV-wave → 30°
9	Oblique incidence of SV-wave at 15°	35.6 kHz	SV-wave → 60°

Table IV. The screw-in depths of the nuts in the *n*th functional unit for directional refraction. (unit: mm).

s_n	case 1	case 2	case 3	case 4	case 5	case 6	case 7	case 8	case 9
s_1	1.22	1.94	1.94	3.81	3.81	3.81	3.81	3.81	3.81
s_2	1.29	1.95	1.98	4.13	4.48	4.83	4.97	4.07	4.52
s_3	1.40	1.98	2.05	4.48	2.17	2.26	2.31	4.36	2.18
s_4	1.52	2.01	2.14	4.83	2.26	2.53	2.75	4.65	2.28
s_5	1.66	2.05	2.27	2.17	2.40	3.05	3.47	4.93	2.45
s_6	1.88	2.10	2.49	2.21	2.68	3.79	4.56	2.17	2.77
s_7	2.30	2.14	2.85	2.26	3.06	4.81	2.24	2.21	3.18
s_8	3.68	2.19	3.86	2.32	3.52	2.25	2.55	2.25	3.71
s_9	5.06	2.27	1.95	2.40	4.11	2.52	3.18	2.30	4.39
s_{10}	0.96	2.36	2.01	2.53	4.82	3.04	4.14	2.36	5.07
s_{11}	0.98	2.49	2.10	2.68	2.21	3.77	2.19	2.44	2.26
s_{12}	1.00	2.65	2.19	2.86	2.32	4.78	2.40	2.55	2.41
s_{13}	1.03	2.85	2.36	3.06	2.53	2.25	2.94	2.68	2.71
s_{14}	1.05	3.16	2.64	3.27	2.86	2.51	3.76	2.83	3.11
s_{15}	1.08	3.86	3.15	3.52	3.27	3.02	4.91	2.99	3.62
s_{16}	1.11	1.94	1.94	3.81	3.79	3.75	2.30	3.16	4.27
s_{17}	1.15	1.95	1.97	4.11	4.46	4.76	2.72	3.35	4.99
s_{18}	1.21	1.97	2.05	4.47	5.08	2.25	3.43	3.56	2.24
s_{19}	1.29	2.01	2.14	4.82	2.26	2.50	4.51	3.81	2.37
s_{20}	1.39	2.05	2.26	2.16	2.39	3.01	2.24	4.06	2.65
s_{21}	1.51	2.10	2.48	2.21	2.67	3.73	2.53	4.35	3.04
s_{22}	1.65	2.14	2.83	2.26	3.04	4.73	3.15	4.64	3.52
s_{23}	1.87	2.19	3.79	2.32	3.50	2.24	4.08	4.92	4.15
s_{24}	2.27	2.27	1.95	2.40	4.09	2.49	2.18	2.17	4.88
s_{25}	3.54	2.36	2.00	2.53	4.80	3.00	2.38	2.21	2.22
s_{26}	5.05	2.48	2.09	2.68	2.21	3.71	2.91	2.25	2.34
s_{27}	0.96	2.64	2.19	2.86	2.31	4.71	3.71	2.30	2.60
s_{28}	0.98	2.84	2.35	3.05	2.52	2.24	4.86	2.35	2.97
s_{29}	1.00	3.15	2.63	3.27	2.85	2.48	2.29	2.44	3.43
s_{30}	1.03	3.82	3.13	3.51	3.25	2.98	2.69	2.55	4.03
s_{31}	1.05	1.94	1.94	3.80	3.77	3.69	3.39	2.68	4.77
s_{32}	1.08	1.95	1.97	4.10	4.44	4.68	4.45	2.83	2.21
s_{33}	1.11	1.97	2.05	4.46	5.07	2.24	2.23	2.98	2.32
s_{34}	1.15	2.01	2.14	4.81	2.25	2.47	2.50	3.15	2.55

Table V. The screw-in depths of the nuts in the *n*th functional unit for wave focusing. (unit: mm).

s_n	central focusing			arbitrary point focusing	
	P-wave incident		SV-wave incident	P-wave incident	
	35.6 kHz	31.4 kHz	35.6 kHz	35.6 kHz	31.4 kHz
s_1	1.94	1.22	3.82	1.94	1.22
s_2	1.95	1.24	3.91	3.73	1.15
s_3	1.95	1.28	4.08	3.11	1.10

s_4	1.97	1.35	4.36	2.84	1.08
s_5	1.99	1.46	4.73	2.69	1.06
s_6	2.04	1.59	2.17	2.58	1.04
s_7	2.09	1.83	2.24	2.53	1.03
s_8	2.15	2.46	2.33	2.49	1.03
s_9	2.24	4.97	2.54	2.49	1.03
s_{10}	2.38	0.97	2.87	2.53	1.03
s_{11}	2.61	1.00	3.32	2.58	1.04
s_{12}	2.97	1.04	3.95	2.69	1.06
s_{13}	4.06	1.08	4.79	2.84	1.08
s_{14}	1.95	1.15	2.23	3.11	1.10
s_{15}	1.99	1.26	2.39	3.73	1.15
s_{16}	2.07	1.45	2.79	1.94	1.22
s_{17}	2.15	1.70	3.35	1.96	1.31
s_{18}	s_{17}	s_{17}	s_{17}	1.99	1.47
s_{19}	s_{16}	s_{16}	s_{16}	2.05	1.66
s_{20}	s_{15}	s_{15}	s_{15}	2.12	2.02
s_{21}	s_{14}	s_{14}	s_{14}	2.19	3.74
s_{22}	s_{13}	s_{13}	s_{13}	2.32	0.95
s_{23}	s_{12}	s_{12}	s_{12}	2.52	0.99
s_{24}	s_{11}	s_{11}	s_{11}	2.82	1.03
s_{25}	s_{10}	s_{10}	s_{10}	3.46	1.07
s_{26}	s_9	s_9	s_9	1.95	1.12
s_{27}	s_8	s_8	s_8	1.98	1.22
s_{28}	s_7	s_7	s_7	2.04	1.37
s_{29}	s_6	s_6	s_6	2.13	1.59
s_{30}	s_5	s_5	s_5	2.22	1.99
s_{31}	s_4	s_4	s_4	2.38	4.33
s_{32}	s_3	s_3	s_3	2.66	0.96
s_{33}	s_2	s_2	s_2	3.12	1.00
s_{34}	s_1	s_1	s_1	5.04	1.05

References

[1] G.C. Ma, C.X. Fu, G.H. Wang, P.d. Hougne, J. Christensen, Y. Lai, P. Sheng, Polarization bandgaps and fluid-like elasticity in fully solid elastic metamaterials, Nat. Commun. 7 (2016), 13536.

[2] Y. Lai, Y. Wu, P. Sheng, Z.Q. Zhang, Hybrid elastic solids, Nat. Mater. 10 (2011), 620-624.

[3] Y. Wu, Y. Lai, Z.Q. Zhang, Elastic metamaterials with simultaneously negative effective shear modulus and mass density, Phys. Rev. Lett. 107 (2011), 105506.

[4] C.L. Holloway, E.F. Kuester, J.A. Gordon, J. O'Hara, J. Booth, D.R. Smith, An overview of the theory and applications of metasurfaces-the two dimensional equivalents of metamaterials, IEEE Antennas Propag. Mag. 54 (2012), 10-35.

[5] N.F. Yu, P. Genevet, M.A. Kats, F. Aieta, J. Tetienne, F. Capasso, Z. Gaburro, Light propagation with phase discontinuities: generalized laws of reflection and refraction, Science 334 (2011), 333-337.

[6] H.T. Chen, A.J. Taylor, N. Yu, A review of metasurfaces: physics and applications, Rep. Prog. Phys. 79 (2016), 076401.

[7] X. Li, X.L. Ma, X.G. Luo, Principles and applications of metasurfaces with phase modulation, Opto-Electronic Eng. 44 (2017), 255.

[8] B. Assouar, B. Liang, Y. Wu, Y. Li, J.C. Cheng, Y. Jing, Acoustic metasurfaces, Nat. Rev. Mats. 3 (2018), 460-472.

[9] B. Liang, J.C. Cheng, C.W. Qiu, Wavefront manipulation by wavefront manipulation by acoustic metasurfaces: from physics and applications, Nanophotonics 7 (2018), 1191–1205.

[10] C. Pfeiffer, A. Grbic, Metamaterial huygens' surfaces: tailoring wave fronts with reflectionless sheets, Phys. Rev. Lett. 110 (2013), 197401.

[11] Y. Li, S. Qi, M.B. Assouar, Theory of metascreen-based acoustic passive phased array, New. J. Phys. 18 (2016), 043024.

[12] Y. Li, B. Liang, Z.M. Gu, X.Y. Zou, J.C. Cheng, Reflected wavefront manipulation based on ultrathin planar acoustic metasurfaces, Sci. Rep. 3 (2013), 2546.

[13] E. Greenfield, M. Segev, W. Walasik, O. Raz, Accelerating light beams along arbitrary convex trajectories, Phys. Rev. Lett. 106 (2011), 213902.

[14] P. Zhang, T.C. Li, J. Zhu, X.F. Zhu, S. Yang, Y. Wang, X.B. Yin, X. Zhang, Generation of acoustic self-bending and bottle beams by phase engineering, Nat. Commun. 5 (2014), 4316.

[15] S.P. Zhao, Y.X. Hu, J. Lu, X.J. Qiu, J.C. Cheng, I. Burnett, Delivering sound energy along an arbitrary convex trajectory, Sci. Rep. 4 (2014), 6628.

[16] X.F. Zhu, K. Li, P. Zhang, J. Zhu, J.T. Zhang, C. Tian, S.C. Liu, Implementation of dispersion-free slow acoustic wave propagation and phase engineering with helical-structured metamaterials, Nat. Commun. 7 (2016), 11731.

[17] W.T. Chen, M. Khorasaninejad, A.Y. Zhu, J. Oh, R.C. Devlin, A. Zaidi, F. Capasso, Generation of wavelength-independent subwavelength Bessel beams using metasurfaces, Light-Sci. Appl. 6 (2017), e16259.

[18] B.Y. Xie, K. Tang, H. Cheng, Z.Y. Liu, S.Q. Chen, J.G. Tian, Coding acoustic metasurfaces, Adv. Mater. 29 (2017), 1603507.

[19] S.D. Zhao, A.L. Chen, Y. S. Wang, C.Z. Zhang, Continuously Tunable Acoustic Metasurface for Transmitted Wavefront Modulation, Phys. Rev. Appl. 10 (2018), 054066.

[20] S.W. Fan, S.D. Zhao, A.L. Chen, Y.F. Wang, B. Assouar, Y.S. Wang, Tunable Broadband Reflective Acoustic Metasurface, Phys. Rev. Appl. 11 (2019), 044038.

[21] Y.F. Zhu, F. Fei, S.W. Fan, L.Y. Cao, K. Donda, B. Assouar, Reconfigurable origami-inspired metamaterials for controllable sound manipulation, Phys. Rev. Appl. 12 (2019), 034029.

[22] A.L. Chen, Q.Y. Tang, H.Y. Wang, S.D. Zhao, Y.S. Wang, Sci. China-Phys. Mech. Astron. 63 (2020), 244611.

[23] H.F. Zhu, F. Semperlotti, Anomalous refraction of acoustic guided waves in solids with geometrically tapered metasurfaces, Phys. Rev. Lett. 117 (2016), 034302.

[24] Y.Q. Liu, Z.X. Liang, F. Liu, O. Diba, A. Lamb, J. Li, Source illusion devices for flexural lamb waves using elastic metasurfaces, Phys. Rev. Lett. 119 (2017), 034301.

[25] J. Zhang, X.S. Su, Y.L. Liu, Y.X. Zhao, Y. Jing, N. Hu, Metasurface constituted by thin composite beams to steer flexural waves in thin plates, Int. J. Solids Struct. 162 (2019), 14-20.

[26] Y.D. Ruan, X. Liang and C.J. Hu, Retroreflection of flexural wave by using elastic metasurface, J. Appl. Phys. 128 (2020), 045116.

[27] L.Y. Cao, Z.C. Yang, Y.L. Xu, B. Assouar, Deflecting flexural wave with high transmission by using pillared elastic metasurface, Smart Mater. Struct. 27 (2018), 075051.

[28] L.Y. Cao, Z.C. Yang, Y.L. Xu, Z.L. Chen, Y.F. Zhu, S.W. Fan, K. Donda, B. Vincent, B. Assouar, Pillared elastic metasurface with constructive interference for flexural wave manipulation, Mech. Syst. Signal Process. 146 (2020), 107035.

[29] L.Y. Cao, Z.C. Yang, Y.L. Xu, S.W. Fan, Y.F. Zhu, Z.L. Chen, B. Vincent, B. Assouar, Disordered Elastic

Journal of Applied Physics

AIP Publishing

Metasurfaces, Phys. Rev. Appl. 13 (2020), 014054.

[30] L.Y. Cao, Y.L. Xu, B. Assouar, Z.C. Yang, Asymmetric flexural wave transmission based on dual-layer elastic gradient metasurfaces, Appl. Phys. Lett. 113 (2018), 183506.

[31] L.Y. Cao, Z.C. Yang, Y.L. Xu, S.W. Fan, Y.F. Zhu, Z.L. Chen, Y. Li, B. Assouar, Flexural wave absorption by lossy gradient elastic metasurface, J. Mech. Phys. Solids 143 (2020), 104052.

[32] J. Zhang, X.S. Su, Y. Pennec, Y. Jing, X.F. Liu, N. Hu, Wavefront steering of elastic shear vertical waves in solids via a composite-plate-based metasurface, J. Appl. Phys. 124 (2018), 164505.

[33] L.H. Zeng, J. Zhang, Y.L. Liu, Y.X. Zhao, N. Hu, Asymmetric transmission of elastic shear vertical waves in solids, Ultrasonics 96 (2019), 34–39

[34] H. Lee, J.K. Lee, H.M. Seung, Y.Y. Kim, Mass-stiffness substructuring of an elastic metasurface for full transmission beam steering, J. Mech. Phys. Solids 112 (2018), 577-593.

[35] X.S. Su, Z.C. Lu, A.N. Norris, Elastic metasurface for splitting SV- and P-waves in elastic solids, J. Appl. Phys. 123 (2018), 091701

[36] M.Y. Zheng, C. I. Park, X.N. Liu, R. Zhu, G.K. Hu, Y. Y. Kim, Non-resonant metasurface for broadband elastic wave mode splitting, Appl. Phys. Lett. 116 (2020), 171903.

[37] M.S. Kim, W.R. Lee, Y.Y. Kim, J.H. Oh, Transmodal elastic metasurface for broad angle total mode conversion, Appl. Phys. Lett. 112 (2018), 241905.

[38] Z.H. Tian, L.Y. Yu, Elastic phased diffraction gratings for manipulation of ultrasonic guided waves in solids, Phys. Rev. Appl. 11 (2019), 024052.

[39] J.J. Rong, W.J. Ye, Multifunctional elastic metasurface design with topology optimization, Acta Materialia 185 (2020), 382–399.

[40] Y.L. Xu, Z.C. Yang, L.Y. Cao, Deflecting Rayleigh surface acoustic waves by a meta-ridge with a gradient phase shift, J. Phys. D: Appl. Phys. 51 (2018), 175106.

[41] Y.F. Wang, Y.Z. Wang, B. Wu, W.Q. Chen, Y.S. Wang, Tunable and active phononic crystals and metamaterials, Appl. Mech. Rew. 72 (2020), 040801.

[42] S.L. Li, J.W. Xu, J. Tang, Tunable modulation of refracted lamb wave front facilitated by adaptive elastic metasurfaces, Appl. Phys. Lett. 112 (2018), 021903.

[43] Y.Y. Chen, X.P. Li, H. Nassar, G.K. Hu, G.L. Huang, A programmable metasurface for real time control of broadband elastic rays, Smart. Mater. Struct. 27 (2018), 115011.

[44] R.Y. Xia, J.L. Yi, Z. Chen, Z. Li, In situ steering of shear horizontal waves in a plate by a tunable electromechanical resonant elastic metasurface, J. Phys. D: Appl. Phys. 53 (2019), 122040.

[45] S.M. Yuan, A.L. Chen, Y.S. Wang, Switchable multifunctional fish-bone elastic metasurface for transmitted plate wave modulation, J. Sound Vib. 470 (2020), 115168.

[46] L.Y. Cao, Z.C. Yang, Y.L. Xu Steering elastic SH waves in an anomalous way by metasurface, J. Sound Vib. 418 (2018), 1-14.

Journal of Applied Physics

PLEASE CITE THIS ARTICLE AS DOI: 10.1063/5.0029045

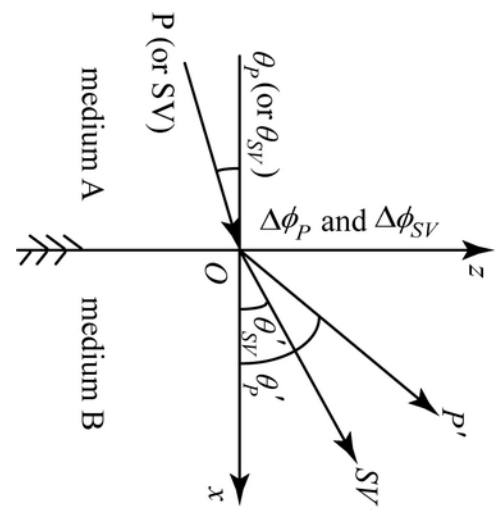

Journal of Applied Physics

AIP Publishing

PLEASE CITE THIS ARTICLE AS DOI: 10.1063/5.0029045

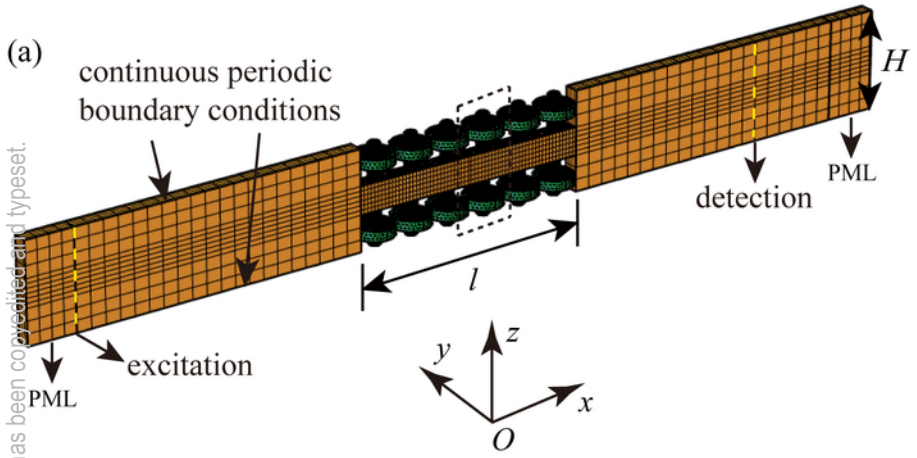

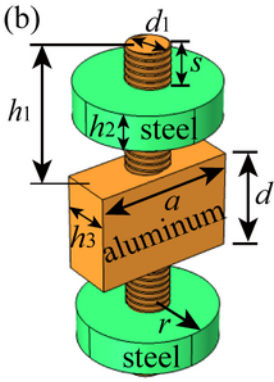

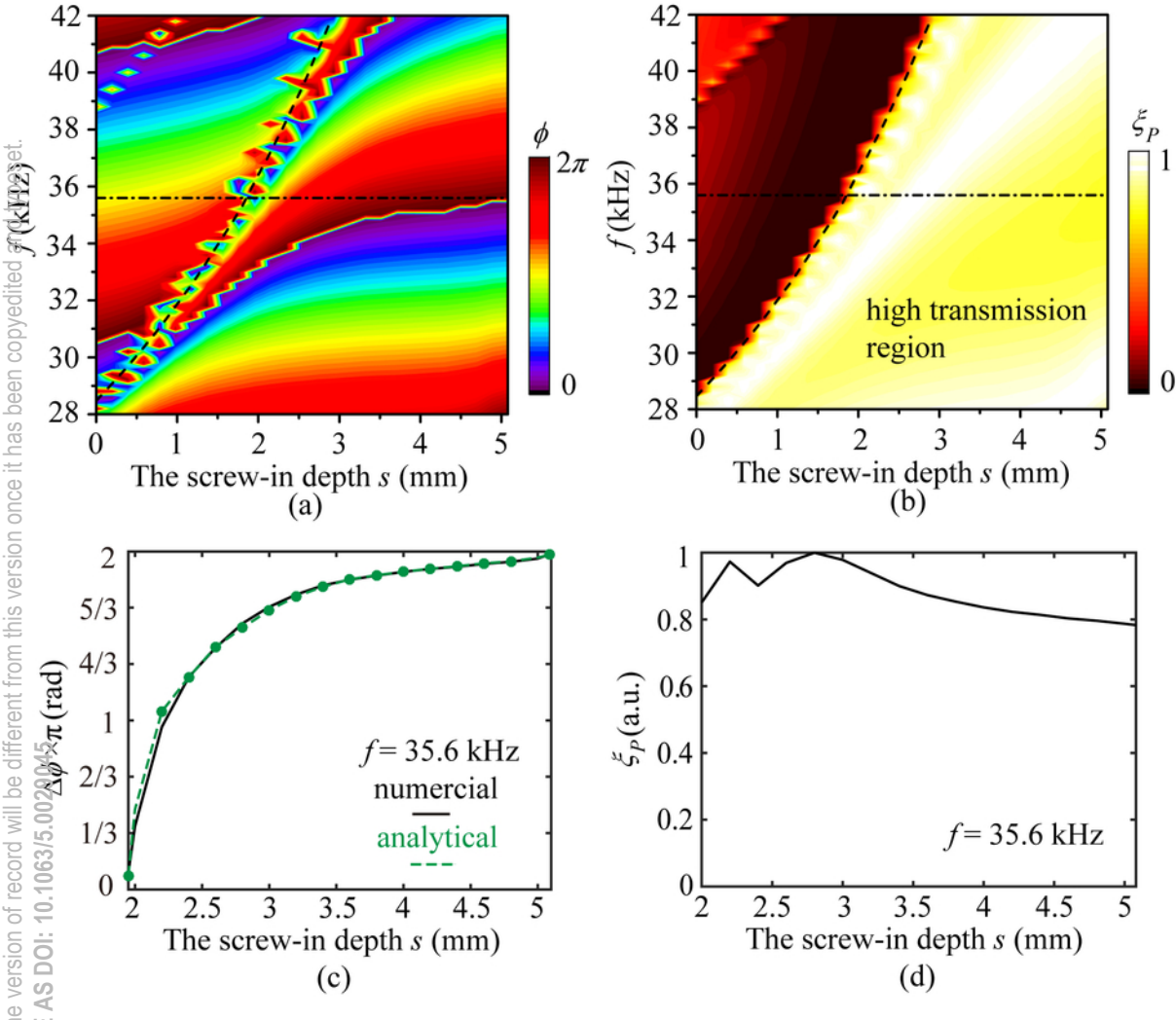

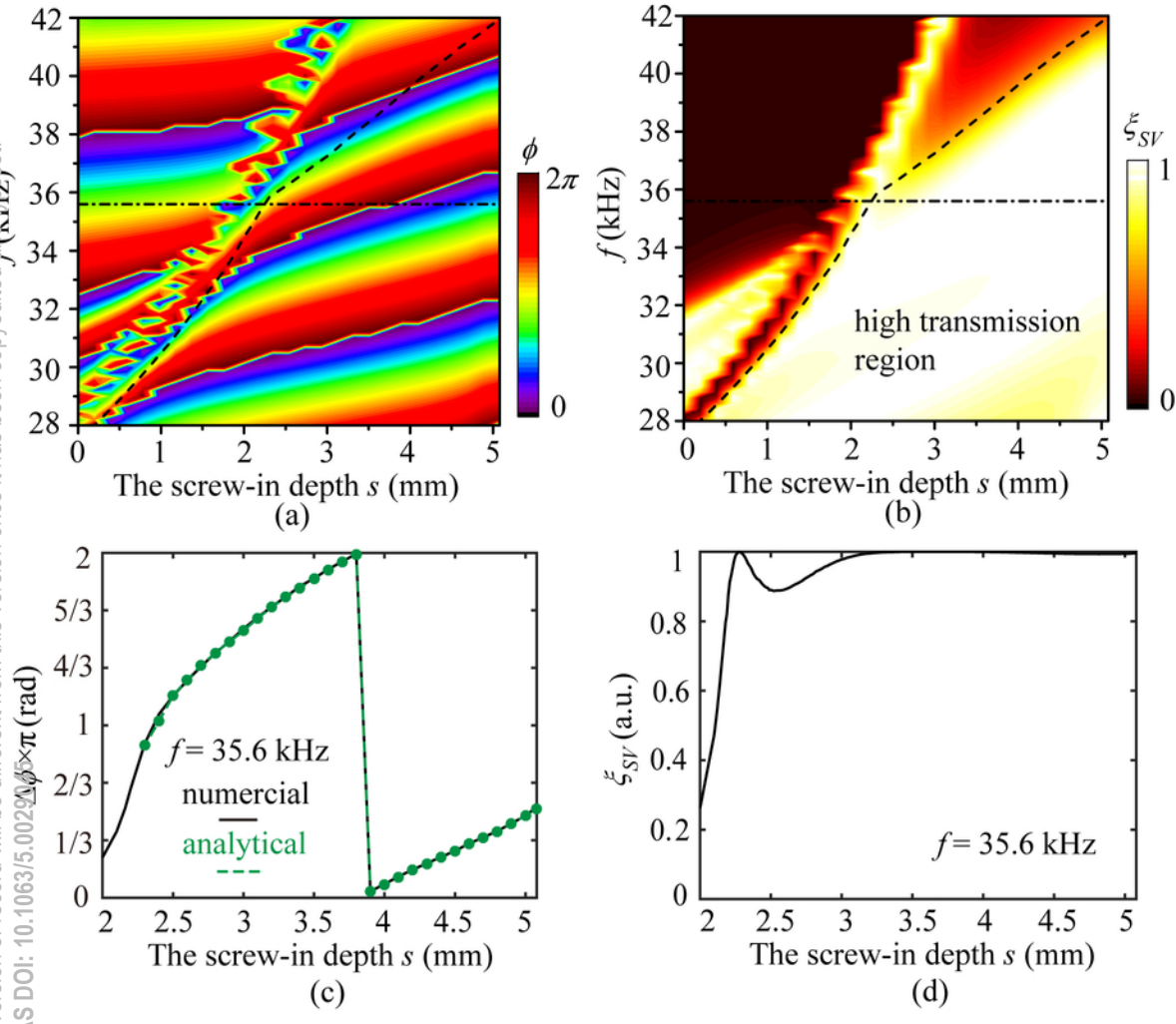

Journal of Applied Physics

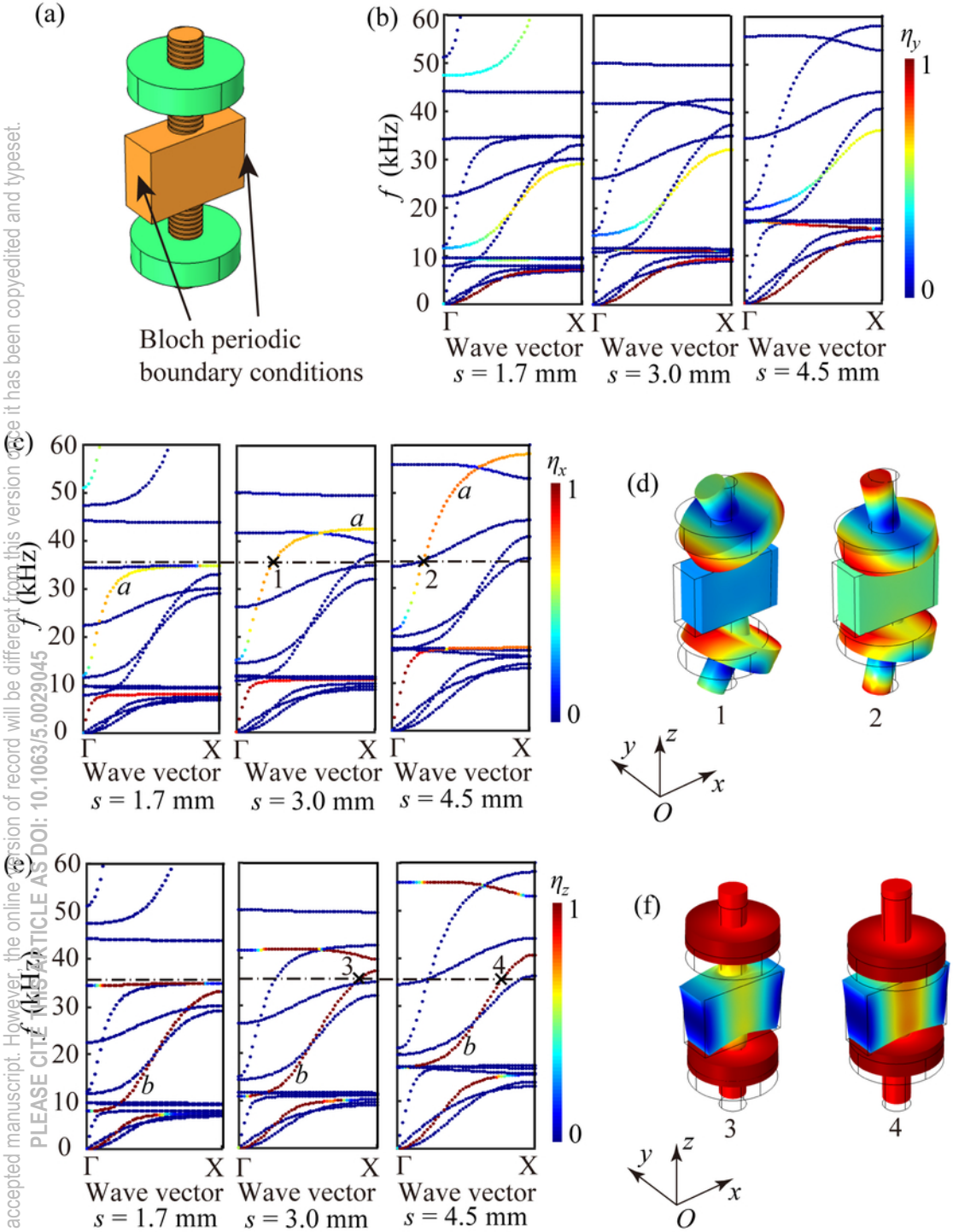

AIP Publishing

Journal of Applied Physics

ACCEPTED MANUSCRIPT

PLEASE CITE THIS ARTICLE AS DOI: 10.1063/5.0029045

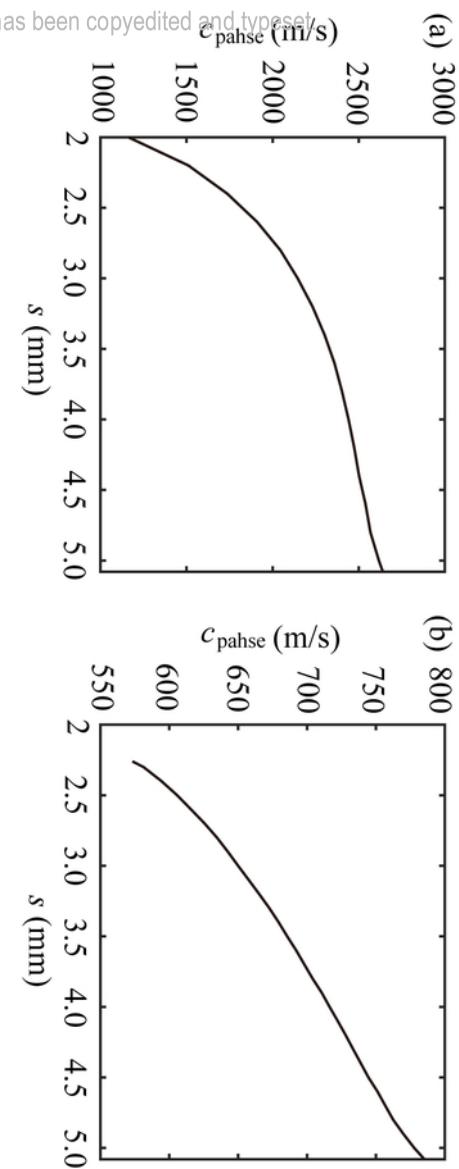

AIP Publishing

Journal of Applied Physics

ACCEPTED MANUSCRIPT

This is the author's peer reviewed, accepted manuscript. However, the online version of record will be different from this version once it has been copyedited and typeset.
PLEASE CITE THIS ARTICLE AS DOI: 10.1063/5.0029045

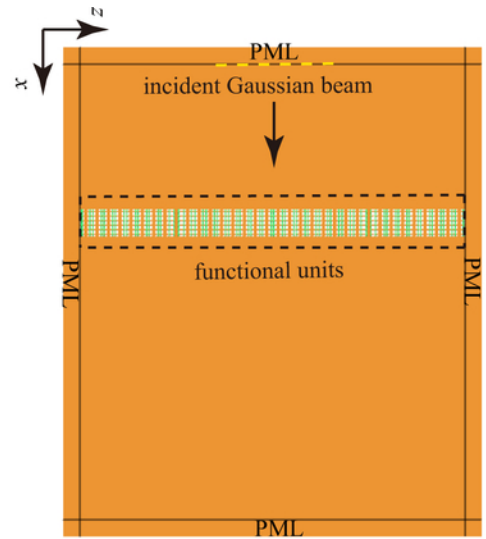

AIP Publishing

Journal of Applied Physics

ACCEPTED MANUSCRIPT

PLEASE CITE THIS ARTICLE AS DOI: 10.1063/5.0029045

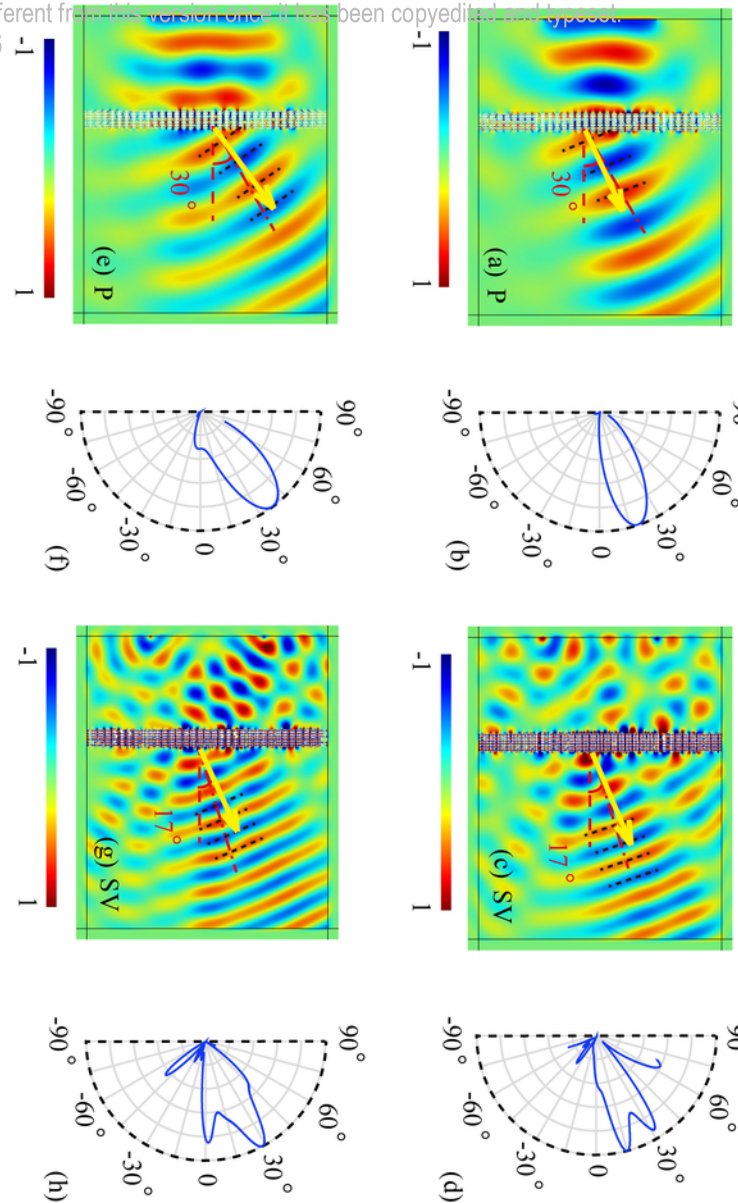

AIP Publishing

Journal of Applied Physics

PLEASE CITE THIS ARTICLE AS DOI: 10.1063/5.0029045

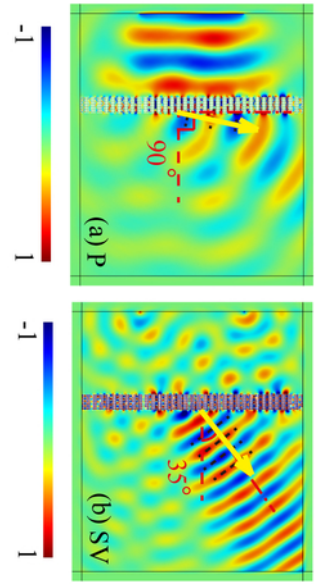

AIP Publishing

Journal of Applied Physics

ACCEPTED MANUSCRIPT

PLEASE CITE THIS ARTICLE AS DOI: 10.1063/5.0029045

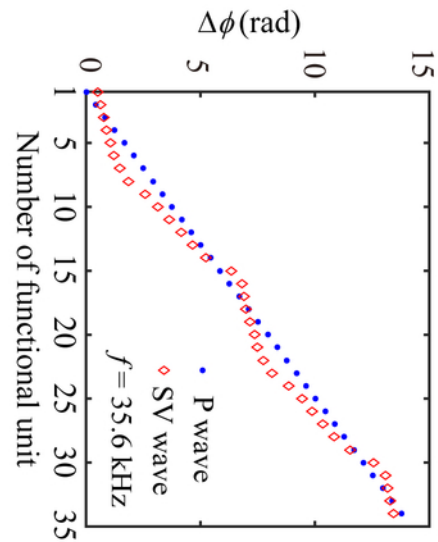

AIP Publishing

Journal of Applied Physics

ACCEPTED MANUSCRIPT

PLEASE CITE THIS ARTICLE AS DOI: 10.1063/5.0029045

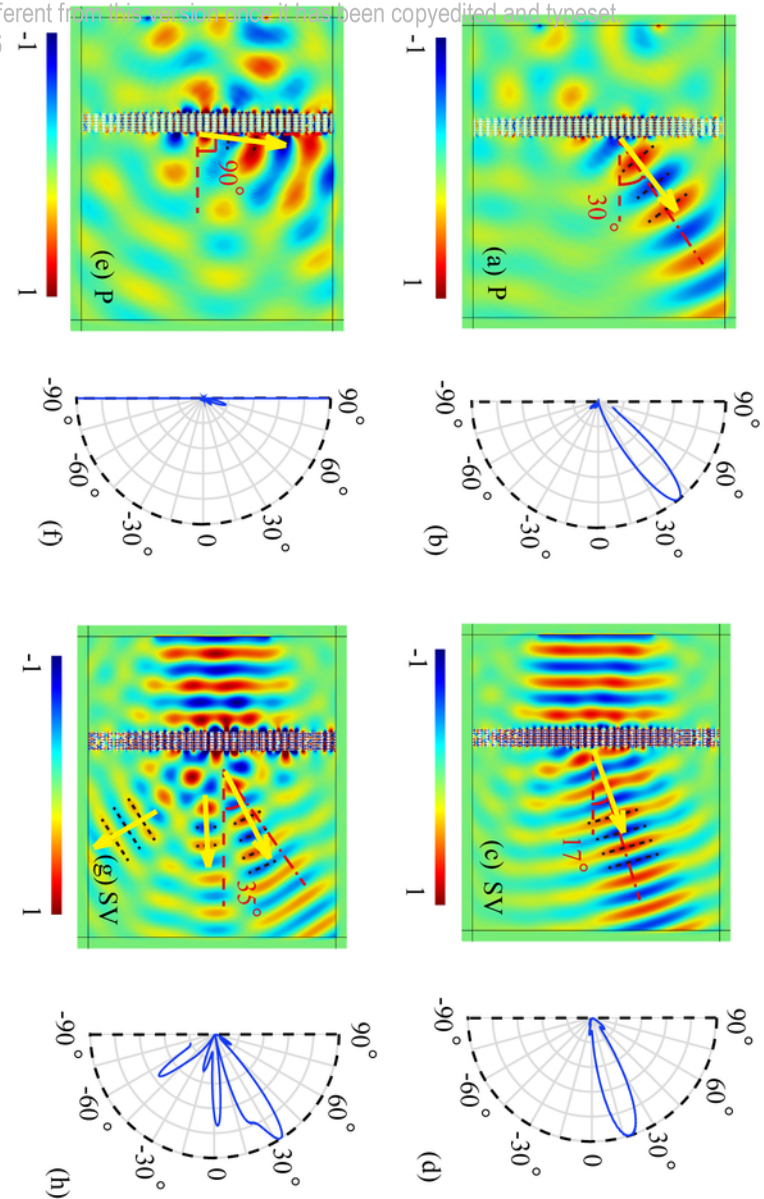

AIP Publishing

Journal of Applied Physics

ACCEPTED MANUSCRIPT

PLEASE CITE THIS ARTICLE AS DOI: 10.1063/5.0029045

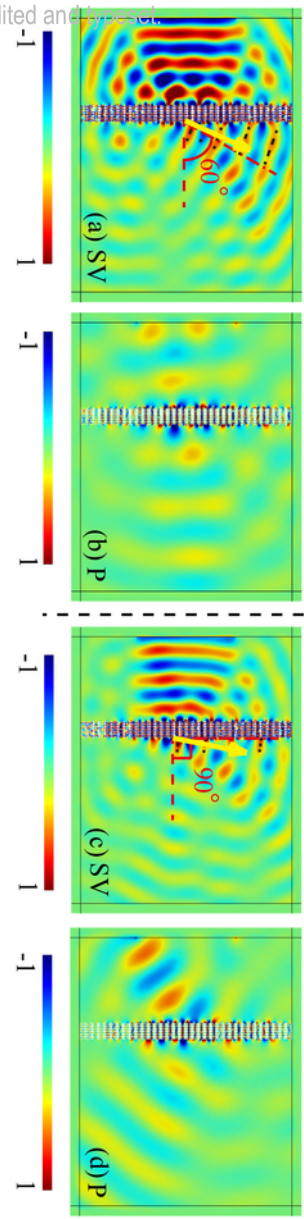

AIP Publishing

Journal of Applied Physics

PLEASE CITE THIS ARTICLE AS DOI: 10.1063/5.0029045

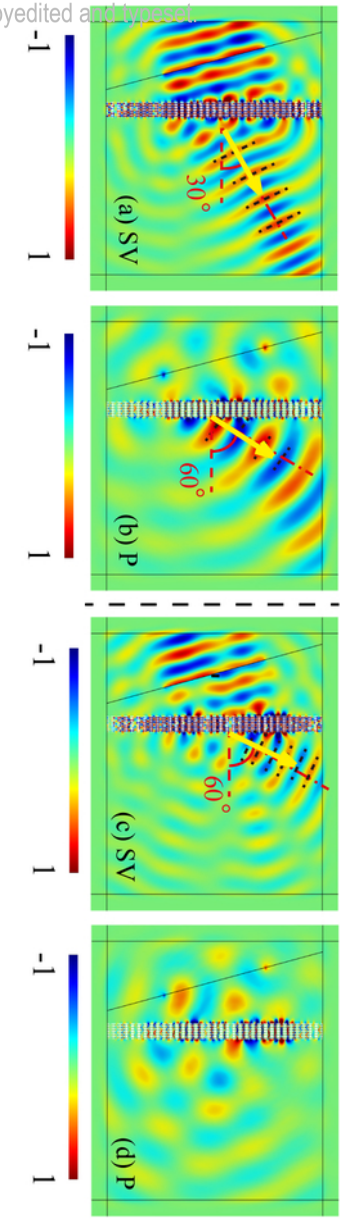

Journal of Applied Physics

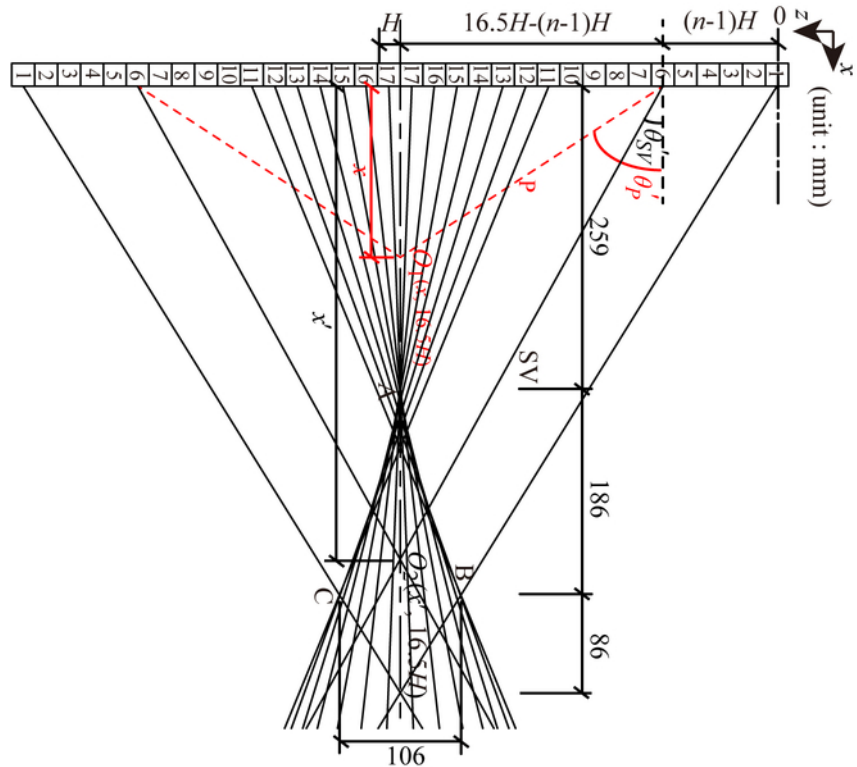

AIP Publishing

Journal of Applied Physics

ACCEPTED MANUSCRIPT

This is the author's peer reviewed, accepted manuscript. However, the online version of record will be different from this version once it has been copyedited and typeset.
PLEASE CITE THIS ARTICLE AS DOI: 10.1063/5.0029045

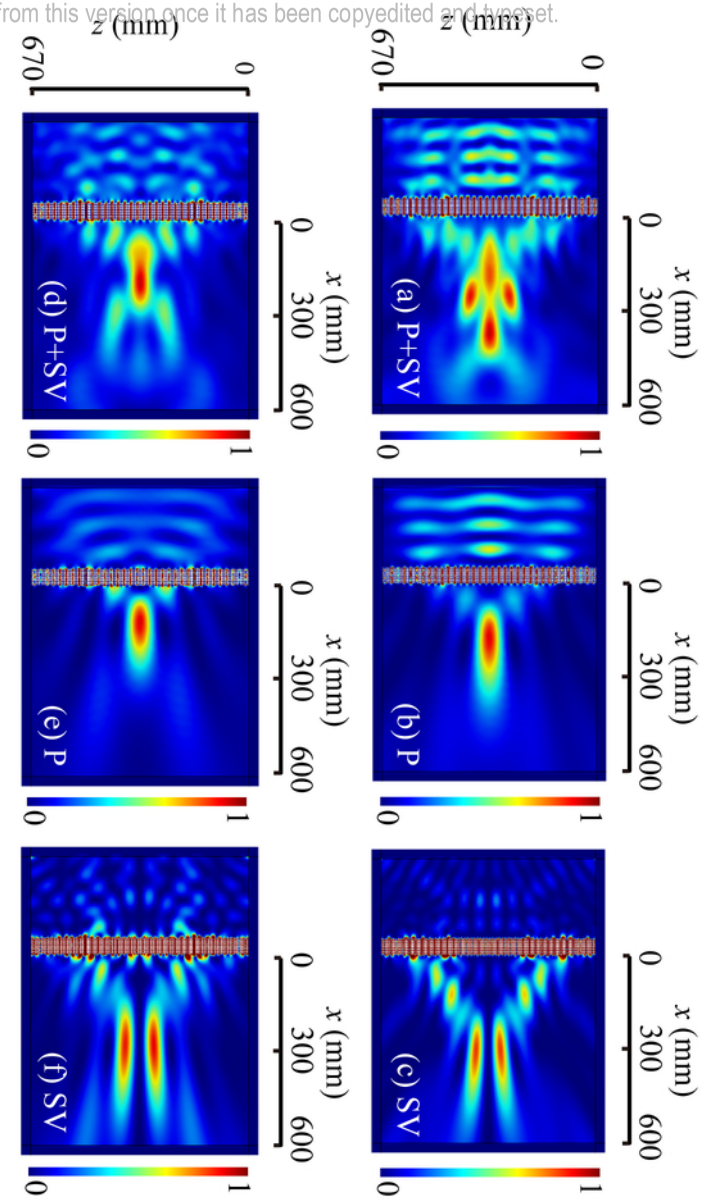

AIP Publishing

Journal of Applied Physics

ACCEPTED MANUSCRIPT

PLEASE CITE THIS ARTICLE AS DOI: 10.1063/5.0029045

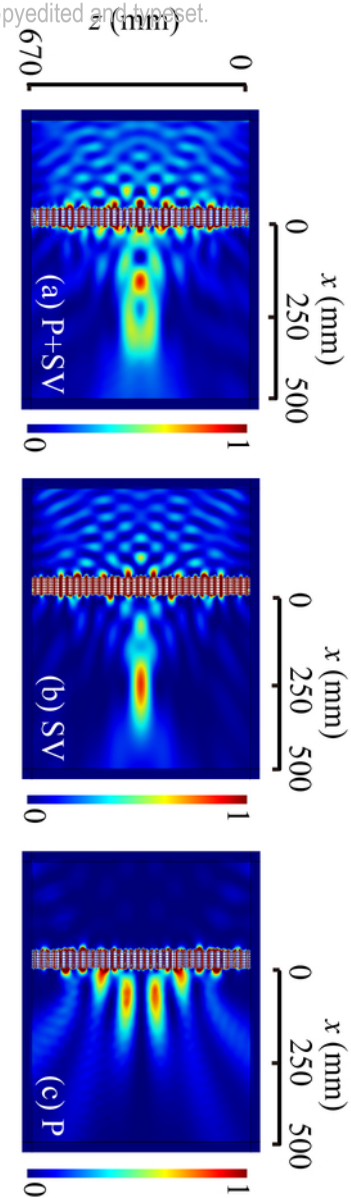

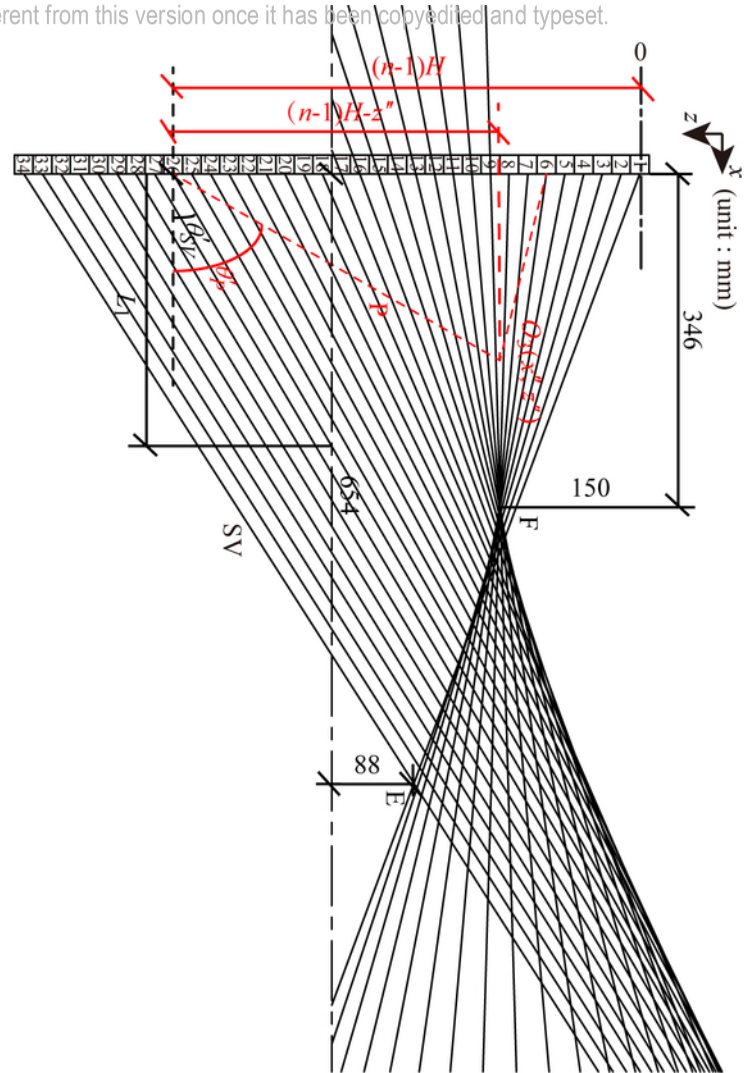

Journal of Applied Physics